

## Quasi-periodic variation during a fast X-ray outburst of a high-mass X-ray binary MAXI 0709–159 / LY CMa observed by NICER

MUTSUMI SUGIZAKI,<sup>1,2</sup> TATEHIRO MIHARA,<sup>3</sup> KOHEI KOBAYASHI,<sup>4</sup> MEGUMI SHIDATSU,<sup>5</sup> WATARU IWAKIRI,<sup>6</sup>  
KEITH GENDREAU,<sup>7</sup> ZAVEN ARZOUMANIAN,<sup>7</sup> DOUGLAS J. K. BUISSON,<sup>8</sup> AND SEAN N. PIKE<sup>9</sup>

<sup>1</sup>*National Astronomical Observatories, Chinese Academy of Sciences, 20A Datun Road, Beijing 100012, People’s Republic of China*

<sup>2</sup>*Advanced Research Center for Space Science and Technology, Kanazawa University, Kakuma, Kanazawa, Ishikawa, 920-1192, Japan*

<sup>3</sup>*RIKEN, Hirosawa, Wako, Saitama, 351-0198, Japan*

<sup>4</sup>*Department of Physics, Nihon University, 1-8 Kanda Surugadai, Chiyoda-ku, Tokyo, 101-8308, Japan*

<sup>5</sup>*Department of Physics, Ehime University, 2-5, Bunkyocho, Matsuyama, Ehime 790-8577, Japan*

<sup>6</sup>*International Center for Hadron Astrophysics, Chiba University, Chiba 263-8522, Japan*

<sup>7</sup>*Astrophysics Science Division, NASA Goddard Space Flight Center, Greenbelt, MD 20771, USA*

<sup>8</sup>*Independent*

<sup>9</sup>*Center for Astrophysics and Space Sciences, University of California, San Diego, CA 92093*

### ABSTRACT

We report on a quasi-periodic variation at  $\sim 1$  Hz during a fast X-ray outburst of a high-mass X-ray binary MAXI J0709–159 / LY CMa observed by the Neutron-star interior composition explorer (NICER). The new X-ray transient MAXI J0709–159 was discovered on 2022 January 25. Due to the transient X-ray behavior characterized by the short (a few hours) outburst duration, rapid ( $\lesssim 1$  s) variability with spectral change, and large luminosity swing from  $10^{32}$  erg s<sup>−1</sup> to  $10^{37}$  erg s<sup>−1</sup>, the object was considered likely to be a supergiant X-ray binary with a neutron star (NS) categorized as a Supergiant Fast X-ray Transient (SFXT). Follow-up NICER and NuSTAR observations confirmed that the position of the new X-ray object is consistent with a Be star, LY CMa, which has been also identified as a B supergiant. We analyzed the NICER data obtained from 3 hours to 6 days after the discovery. The light curve reveals that the X-ray activity continued for  $\sim 7$  hours in sparse short flares, each lasting  $\lesssim 100$  seconds, and the luminosity instantaneously reached up to  $\sim 1 \times 10^{38}$  erg s<sup>−1</sup>. The light-curve and spectral features reasonably agree with those expected from accretion of a clumpy stellar-wind onto a magnetized NS. The variability power spectrum during the brightest flare shows a broad peak at 1.1 Hz resembling a quasi-periodic oscillation (QPO). If the QPO is attributed to the Keplerian orbital frequency at the inner edge of a transient accretion disk truncated by the NS magnetosphere, the NS surface magnetic field is estimated to be  $\sim 10^{12}$  G.

**Keywords:** X-rays: individual (MAXI J0709–159, LY CMa, HD 54786) — stars: Be — stars: neutron — X-rays: binaries

### 1. INTRODUCTION

MAXI J0709–159 (hereafter MAXI J0709; Serino et al. 2022) is a new X-ray transient discovered on 2022 January 25 near the Galactic plane at  $(l, b) = (229^\circ.3, -2^\circ.3)$  by the Monitor of All-sky X-ray Image (MAXI; Matsuoka et al. 2009) onboard the International Space Station (ISS). From the observed transient behavior characterized by the short ( $\lesssim 3$  hours) activity duration, rapid ( $\lesssim$  a few seconds) variability accompa-

nied with spectral changes, and large luminosity swing by a factor of  $\gtrsim 10^4$  from the quiescence to the outburst peak, the object was considered likely to be a Supergiant Fast X-ray Transient (SFXT), a possible subclass of supergiant X-ray binaries (SgXBs) accompanied by magnetized neutron stars (NSs) (Kobayashi et al. 2022).

By coordinated follow-up observations with the Neutron star Interior Composition ExploreR (NICER; Gendreau et al. 2016) and the Nuclear Spectroscopic Telescope Array (NuSTAR; Harrison et al. 2013), MAXI J0709 was successfully identified with a new X-ray object located at the position consistent with an optical

companion, LY CMa, also known as HD 54786 (Iwakiri et al. 2022; Negoro et al. 2022), located at the distance of  $D = 3.03^{+0.31}_{-0.27}$  kpc (Bailer-Jones et al. 2021). LY CMa has been categorized as a Be star due to the presence of hydrogen emission lines (Chojnowski et al. 2015) but is also known as a B supergiant (B1.5b) in the optical spectral classification (Houk & Smith-Moore 1988). Hence, optical follow-up observations were carried out. The results confirmed that the optical spectra had a broad H $\alpha$  emission line suggesting that the circumstellar Be disk was formed (Nesci 2022; Bhattacharyya et al. 2022; Sugizaki et al. 2022; Shidatsu et al. 2025). These observed X-ray and optical features suggest that the optical counterpart, LY CMa, certainly has a complex circumstellar medium (CSM) embracing the Be disk as well as clumpy stellar winds (Sugizaki et al. 2022). Also, Bhattacharyya et al. (2024) proposed that the object is on an intermediate evolution phase between Be X-ray binaries (BeXBs) and SgXBs from its optical color-magnitude location.

SFXTs are proposed as a possible subclass of SgXBs for those members that sporadically (once every few months to several years) exhibit short-duration (several hours) outbursts (e.g. Sguera et al. 2006; Bozzo et al. 2015; Romano et al. 2013; Sidoli & Paizis 2018; review in Kretschmar et al. 2019). So far, about a dozen SFXTs and their candidates have been identified in our Galaxy. Because a few of them were found to show coherent X-ray pulsations, these objects are considered likely to be binary systems hosting magnetized NSs. However, physical mechanisms that enable such extremely short outbursts have not been well understood. These features in X-ray activity are quite different from those of classical SgXBs that usually exhibit persistent X-ray emission. From the sporadic and short-duration outburst activities, mass accretion onto the NS is thought to be induced by interaction with clumpy stellar winds. The large intensity swing by a factor of  $\sim 10^5$  from the quiescence to the outburst peak in the short time period requires some mechanisms to inhibit mass accretion such as magnetic and/or centrifugal barriers (Grebenev & Sunyaev 2007; Bozzo et al. 2008). To explain this, Bozzo et al. (2008) proposed a hypothesis that the NS should have a strong surface magnetic field  $B_s \sim 10^{13} - 10^{14}$  G like a magnetar. On the other hand, Shakura et al. (2013, 2014) proposed another scenario that these objects are slow-rotating NSs with regular  $B_s$  ( $\sim 10^{12}$  G) and the sporadic outbursts result from instabilities of quasi-spherical accretion shells formed around the NS magnetosphere.

MAXI J0709 is a unique high-mass X-ray binary (HMXB) that exhibited transient behavior like SFXTs but has a stellar companion which shows properties of

Be stars as well as B supergiants. Hence, it can become a critical sample to address questions regarding SFXTs. Usually, observations of SFXTs in their active outburst phase are difficult because their occurrence is very rare and unexpected. The NICER observations of MAXI J0709, which started just 3 hours after the discovery, were enabled by the coordinated operation between MAXI and NICER, two astronomical experiments on the ISS. The NICER data provides us a great opportunity to study the rapid variability with large photon statistics and excellent time resolution that had not been realized before.

In this paper, we present detailed analysis of the NICER observations of MAXI J0709. We describe the NICER observations in section 2, and the data analysis and results in section 3. Based on the results, we discuss possible mechanisms for the observed fast X-ray variability in section 4. Throughout the paper below, we provide errors on observed parameters at 90% confidence limits of statistical uncertainties, unless otherwise specified.

## 2. OBSERVATIONS AND DATA REDUCTION

NICER is an X-ray astronomical mission that has been carried out on the ISS since 2017. The main science instrument, X-ray Timing Instrument (XTI), consists of 56 X-ray concentrator optics (XRC) and matching silicon drift detectors, covering the 0.2–12 keV band with large effective area (1700 cm<sup>2</sup> at 1 keV). The detectors have a capability of recording every X-ray event with unprecedented time resolution ( $\lesssim 300$  ns) and energy resolution similar to standard silicon-based semiconductor detectors (137 eV at 6 keV) (Gendreau et al. 2016).

The first NICER observation of MAXI J0709 was performed to identify the new X-ray transient detected by MAXI on 2022 January 25 under the MAXI-NICER coordinated observation program. At UT 13:42, approximately 3 hours after the first MAXI detection, the NICER/XTI grid scan observation covering the entire MAXI error region encircled by a radius of  $\sim 0^\circ 25'$  started. At UT 13:54, the new X-ray object was successfully confirmed and the source position was determined with  $3'$  accuracy (appendix A). Subsequently, additional follow-up observations to monitor the source activity were carried out. Table 1 lists all of the NICER observations performed in the five days after the discovery. The source position was later refined with  $10''$  accuracy by the NuSTAR observation and then the optical counterpart of LY CMa was identified (Sugizaki et al. 2022).

We analyzed all NICER data including grid-scan data listed in table 1. The data reduction and analysis were performed with the standard analysis tools NICER-

**Table 1.** Logs of NICER MAXI J0709–159 observations performed in 2022 January.

ObsID	Start Time (UTC)	Stop Time (UTC)	Exp. (s)
4202520101 <sup>a</sup>	Jan 25 13:54:11	Jan 25 23:27:07	7174
4202520102	Jan 26 00:35:34	Jan 26 22:39:46	12728
4202520103	Jan 26 23:49:13	Jan 27 03:21:20	3519
4202520104	Jan 28 00:35:53	Jan 28 00:49:02	789
4202520105	Jan 29 02:55:54	Jan 29 11:06:40	4830
4202520106	Jan 30 08:27:34	Jan 30 16:26:23	2016

<sup>a</sup>For the first 30 minutes, a grid scan observation was done.

DAS version v011a released as a part of HEASOFT version 6.32.1 and the calibration files CALDB version xti20221001. We first reprocessed all event data with a standard tool `nicerl2` and screened them with typical filtering criteria: the pointing offset is less than  $3'$  of the source position uncertainly (appendix A), the pointing direction is more than  $40^\circ$  away from the bright Earth limb, more than  $30^\circ$  away from the dark Earth limb, the ISS is located outside the South Atlantic Anomaly (SAA), and the geomagnetic cutoff rigidity (COR) is  $> 1.5$  GeV/c. Events measured by two noisy detectors, FPMs 34 and 14, were also filtered out. We started all data analysis in the following sections with the obtained cleaned data.

### 3. ANALYSIS

#### 3.1. Overall light curve

To overview the entire outburst profile, we first extracted light curves of all NICER data and plotted them with the MAXI/GSC (Gas Slit Camera; Mihara et al. 2011; Sugizaki et al. 2011) data, which obtained from the MAXI quick-look website<sup>10</sup>. Figure 1 (top) shows the obtained NICER 0.5–10 keV light curve with 1-s time bins and the MAXI 2–10 keV data taken every 90-min ISS orbital cycle for 7 days from 1 day before the first MAXI detection. There, the scales of X-ray intensities measured by two instruments, NICER/XTI and MAXI/GSC, are normalized by assuming the typical power-law spectral model with a photon index  $\Gamma = 1$  and an absorption column density  $N_H = 10^{23}$  cm<sup>-2</sup>, which were determined in the spectral analysis (section 3.4). In this power-law model, the NICER peak count rate,  $\sim 500$  cts s<sup>-1</sup>, corresponds to the 0.5–10 keV flux

of  $\sim 1 \times 10^{-8}$  erg cm<sup>-2</sup> s<sup>-1</sup>. Hereafter, the time from the first MAXI source detection at  $t_0 = 2022-01-25$  10:42:40 (UTC) is denoted as  $t$ .

The combined NICER and MAXI light curves reveal that the source exhibited several flares only in the initial 0.3 days  $\simeq 7$  hours. After  $t = 0.3$  d, no significant X-rays from the target source have been detected with either NICER or MAXI. At  $t = 3.5$  d, a NuSTAR observation of 18 ks exposure was carried out and the new X-ray object with the 2–10 keV flux of  $6 \times 10^{-13}$  erg cm<sup>-2</sup> s<sup>-1</sup> was detected (Sugizaki et al. 2022). This means that the source intensity decreased by a factor of  $10^{-4}$  in 3.5 days. The time interval of the NuSTAR observation is illustrated in the figure 1 (top).

Figure 1 (middle) shows the close-up view of the initial 0.3 days. Because both MAXI and NICER are ISS-payload missions, the good-time intervals (GTIs) of these observations are synchronized with the ISS orbital period of  $\sim 90$  minutes ( $= 5400$  s). Hence, we named the three GTIs of the NICER data in this 0.3 days as GTI-A, B, C, as labeled in the figure. As seen in the figure, data taken at the same time or close in time by MAXI and NICER are roughly consistent.

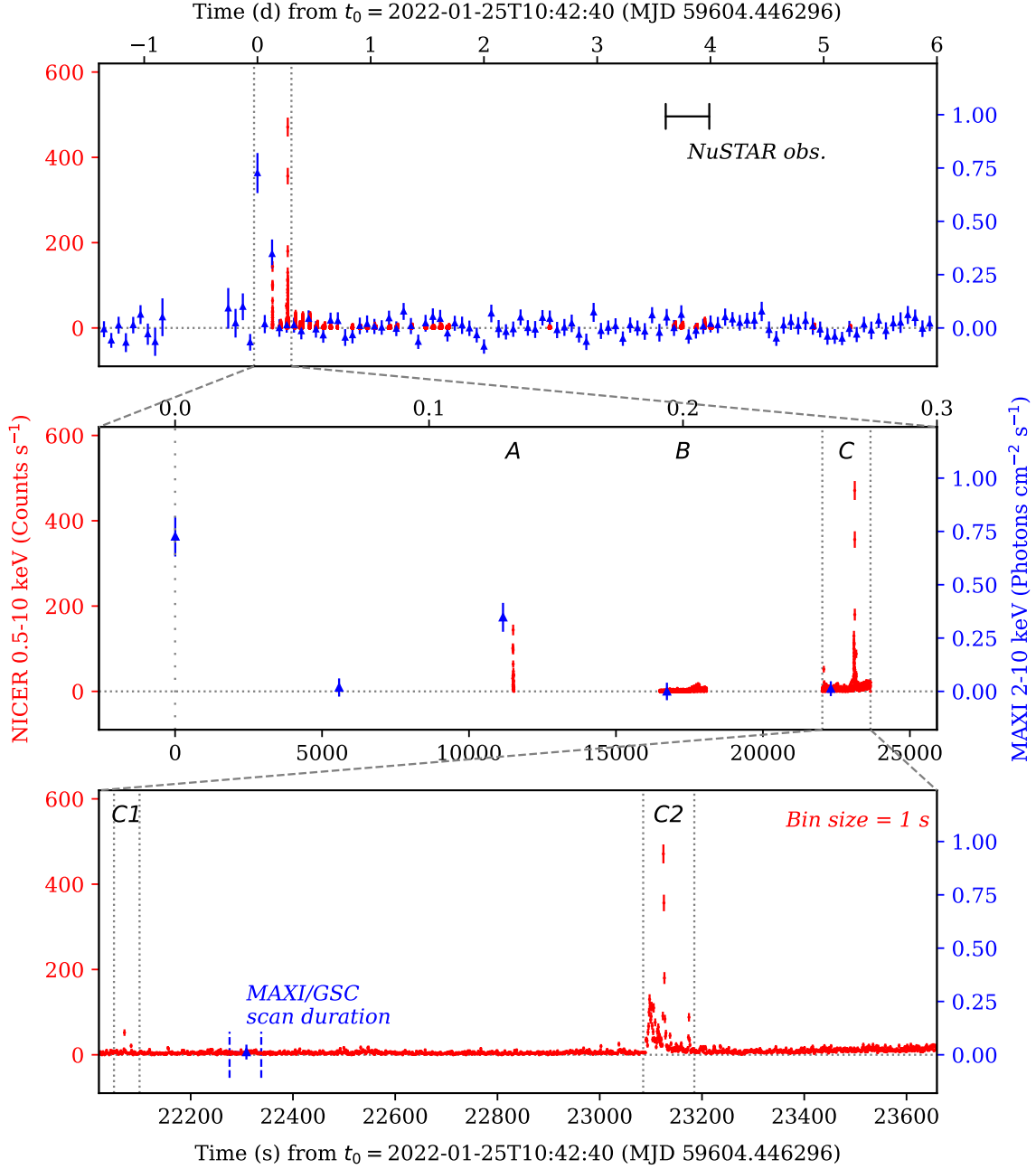
The observation of the GTI-A was performed as a part of the grid scan to identify the new transient. The position of the later identified object, LY CMa, was observed only for 37 s from  $t = 11491$  s to 11528 s. The NICER light curves (red dot marks) shows a remarkable X-ray flare with a large variability. At  $t = 11150$  s, i.e. 340 s before the GTI-A, MAXI/GSC scanned the source position and detected a significant flare with the same activity level (blue triangle marks). This suggests that this flare would continue over the two observations separated by 340 s. In the next GTI-B covering 1592 s from  $t = 16488$  s to 18080 s, no significant X-rays over the backgrounds were detected. However, in the GTI-C of 1640 s from  $t = 22020$  s to 23660 s, bright X-ray flares were detected again for a part of the interval. The peak intensity in the GTI-C was highest among all of the NICER data and comparable to that at the initial source onset ( $t = 0$ ) observed by MAXI.

Figure 1 (bottom) shows the further close-up view of the GTI-C. The flaring activities appeared only in a few short intervals of  $\lesssim 100$  s. The brightest flare at around  $t = 23100$  s exhibits rapid variations in time scales shorter than the 1-s bin size. Hereafter, we refer to the two clear flaring periods labeled in the figure as C1 and C2.

#### 3.2. Rapid variability and hardness ratio

From the overall light curve of figure 1, we found that the X-ray activity of MAXI J0709 appeared only until

<sup>10</sup> <http://maxi.riken.jp>



**Figure 1.** MAXI J0709–159 X-ray light curves observed by NICER in 0.5–10 keV band (red) and MAXI in 2–10 keV band (blue). The NICER data represents count rate including backgrounds every 1-s time bin. MAXI data are obtained from the public web site, which provides estimated photon flux every scan transit of  $\sim 40$  s assuming the power-law spectrum of photon index  $\Gamma = 2$ . X-axis labels at the top and bottom on each panel represent the elapse time from the first source detection at  $t_0 = \text{UTC } 2022 \text{ January } 25 \text{ 10:42:40 (MJD 59604.446296)}$  in units of day and second, respectively. **(Top)** Overall profiles of 7 days including all NICER observations from one day before the first MAXI detection, annotated with the NuSTAR observation period. **(Middle)** First 6 hours including all significant X-ray flares observed by NICER. Labels A, B, C represents three good-time intervals of NICER data separated by the 90-min ISS orbital period. **(Bottom)** 20 minutes of the NICER GTI-C including the brightest flare in the NICER data. Labels C1, C2 represent periods of two remarkable flares.

$t = 0.3$  d ( $\simeq 7$  h) with several short flare-up episodes, each lasting only  $\lesssim 100$  s. Hence, we next investigated the details of each flare.

Figure 2 shows the light curves of three remarkable flaring periods, GTI-A (hereafter simply A), C1 and C2, labeled in figure 1, for 50 s, 50 s and 100 s, respectively, with 0.1-s time bins. These profiles reveal that each flare consists of short spikes of a few seconds with a similar triangular shape. The flare C2 includes the brightest interval of a few seconds with the count rate over 200  $\text{cts s}^{-1}$ , which is significantly higher than that in the rest of the period. We named this brightest 4 seconds as C2a, as labeled in figure 2, and the remaining C2 except C2a as C2\*. The peak count rate of  $\sim 1000$   $\text{cts s}^{-1}$  in the 0.1-s time bin is twice as high as  $\sim 500$   $\text{cts s}^{-1}$  in the 1-s time bin (figure 1), indicating that the variation time scale is shorter than 1 s.

To investigate the spectral change synchronized with the intensity variation, we plot the 4–10 keV to 0.5–10 keV hardness ratio of every 0.5-s time bin on the light curves in figure 2 (with blue dot). Also, the hardness-intensity diagram is shown in figure 3, where data of three distinctive flaring periods, A, C2a and C2\*, are marked with different colors and symbols. We cannot see any clear correlation between the hardness and intensity. On the other hand, the hardness of the flare A is slightly higher than that of the flare C2 (including both C2a and C2\*).

### 3.3. Variability power spectrum

To study time scales of the fast variability seen in figure 2 and also search for possible coherent pulsations, we investigated the power-density spectra (PDS). In the beginning, we converted all event times, which were recorded on the ISS, into the arrival times at the solar system barycenter using `barycorr`, a standard tool in HEASOFT, with the ISS orbit data and assuming that all X-ray events came from the direction of the identified object, LY CMa. We used the Python package `stingray` (Huppenkothen et al. 2019a) to calculate the PDS from the event data.

We analyzed data of three GTIs, A, B, and C, defined in section 3.1 as shown in figure 1 (middle), separately. Because the GTI-B shows no X-ray activity, the result can be used as the reference for background data. We first calculated PDS for every time segment divided by a specific length from light-curve data in 0.5-ms time bin, i.e. in the frequency range up to 1 kHz. The lower end of the frequency range depends on the segment length. Considering the length of each GTI, we divided the GTI-A of 37 s into two 18.5-s segments, the GTI-B of 1592 s into four 398-s segments, and the GTI-C of 1640 s into

four 410-s segments. Then, we calculated the average PDS of each GTI.

Figure 4 (a) shows the obtained PDSs of the three GTIs with Leahy normalization (Leahy et al. 1983) and logarithmical rebinning for visual clarity. As a representative example, an unbinned PDS of the GTI-C is shown together. No significant signal of coherent pulsations was detected. The PDSs of GTI-A and GTI-C, which have significant X-ray activities, show a similar profile over the background estimated from the GTI-B data. The broad enhanced structure below 0.5 Hz corresponds to a cycle of short spikes every  $\sim 10$  s. In addition, an isolated peak at  $\sim 1$  Hz with a certain width like quasi-periodic oscillation (QPO) is clearly seen in the GTI-C. In the higher frequency above  $\sim 1$  Hz, all PDSs are consistent with a constant = 2 corresponding to the Poisson fluctuation in the Leahy normalization.

To examine possible time variation of the QPO-like feature during the GTI-C, we calculated PDSs for 4 divided subsegments of (i) before the bright-flare period C2, (ii) the first half of C2, (iii) the second half of C2 including the flare peak, and (iv) after C2. Figure 4 (b) shows the obtained PDSs. The QPO-like signal can be recognized in both first half and second half of C2 at the same frequency  $\sim 1$  Hz, but not anywhere else. Therefore, the feature is considered to associate with the C2 flare.

To characterize the QPO-like feature, we fitted the PDS profile around the peak from 0.25 Hz to 5 Hz with a model consisting of a Lorentzian function, a power-law continuum, and a constant offset = 2 for the Poisson fluctuation, which has been often used for QPOs in various X-ray binaries (e.g. Belloni et al. 2002). The fit is accepted with the best-fit Lorentzian parameters of the centroid frequency  $\nu_0 = 1.14 \pm 0.03$  Hz, half-width at the half-maximum  $\Delta = 0.12 \pm 0.02$ , integrated fractional RMS =  $0.58 \pm 0.05$ , and the continuum power-law index of  $-1.59^{+0.16}_{-0.20}$ . The quality factor for the QPO feature is estimated as  $Q = \nu_0/2\Delta = 4.8$ . In the inset of figure 4, the best-fit model is shown on the data.

### 3.4. Energy spectra

We investigated X-ray energy spectra of individual flare periods. We used the standard NICER analysis script `nicer13-spect` to extract source spectra, background spectra predicted by SCORPEON model<sup>11</sup>, and energy response functions for specified GTIs. We performed model fitting on XSPEC version 12.13.1 (Arnaud 1996) based on the  $W$ -statistic, a modified version of  $C$ -

<sup>11</sup> [https://heasarc.gsfc.nasa.gov/docs/nicer/analysis\\_threads/scorpeon-overview/](https://heasarc.gsfc.nasa.gov/docs/nicer/analysis_threads/scorpeon-overview/)



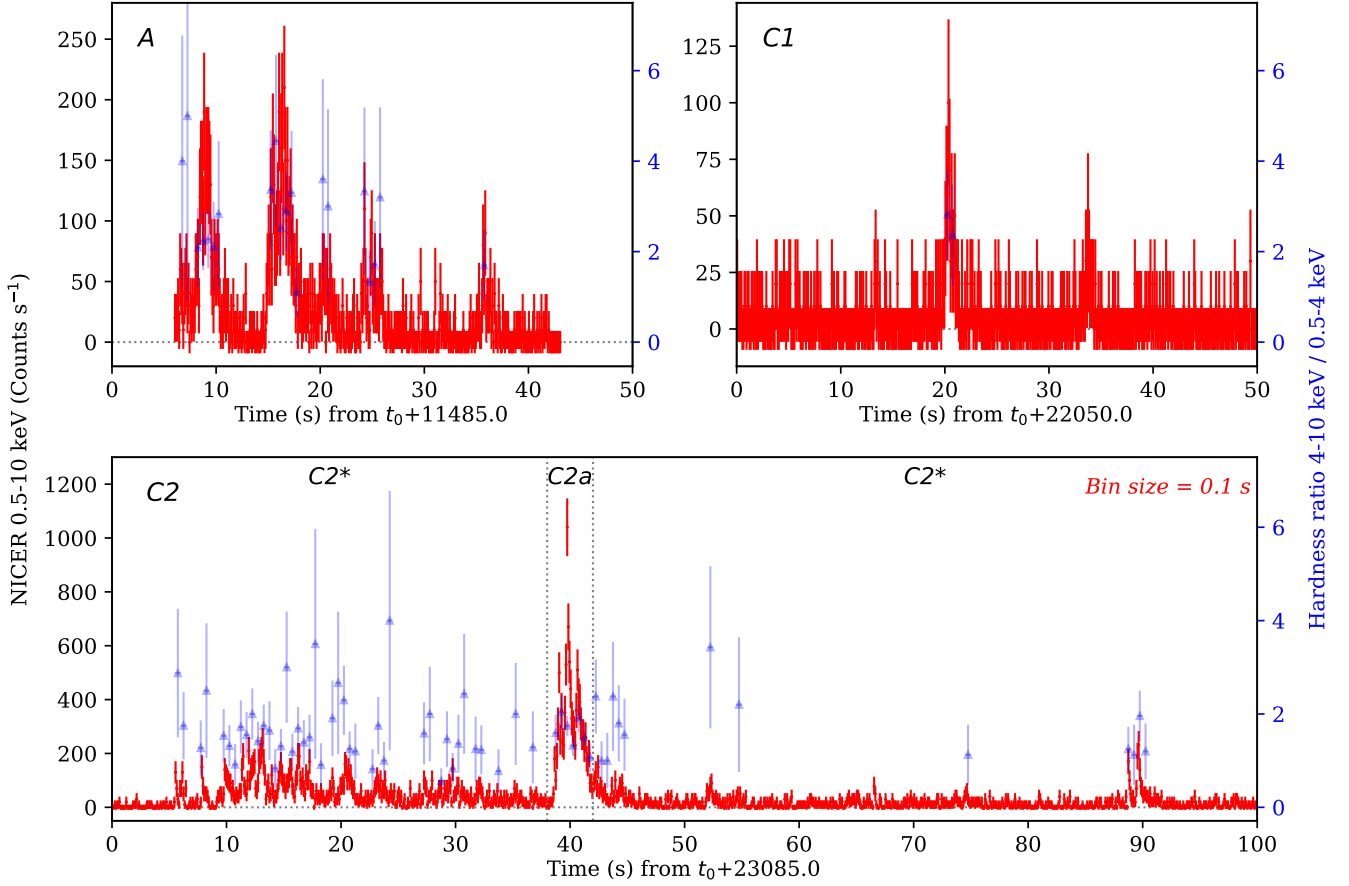


**Figure 2.** NICER 0.5–10 keV light curve in 0.1-s time bin (red) and hardness ratio variation of 4–10 keV to 0.5–4 keV in 0.5-s time bin (blue) for three flaring periods of A (50 s), C1 (50 s), and C2 (100 s), labeled in figure 1.

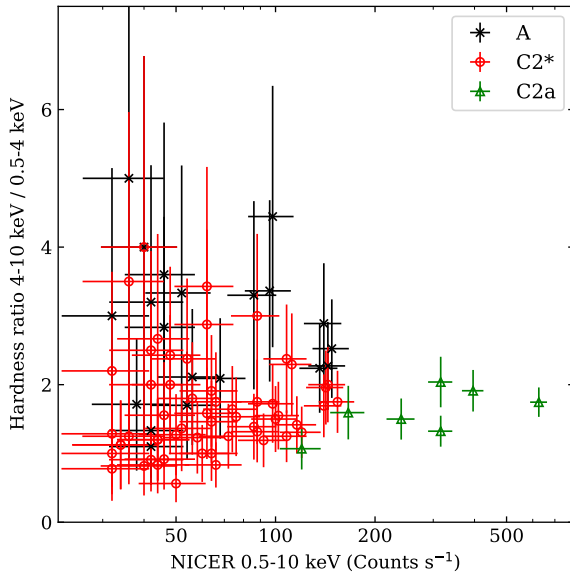


**Figure 3.** Hardness-intensity diagram during the two flares of A and C2, shown in figure 2.

statistic (Cash 1979) taking into account the background contributions. There, using the `error` command or the `eqwid` command (for equivalent width) in XSPEC, we calculated model-parameter errors corresponding to an increase of 2.7 in the fit statistic  $W$ , which are equivalent to 90% confidence limits.

Figure 5 shows the obtained energy spectra including backgrounds for three distinctive flaring periods, A, C2\* (C2 except C2a peak) and C2a, which have been defined in section 3.2 as in figure 2. We first fitted all the spectra with a power-law model with interstellar-medium (ISM) absorption employing the Tuebingen-Boulder absorption model (`tbabs`) with the solar abundance given by Wilms et al. (2000) and background models predicted by the default SCORPEON parameters. As the results, we obtained similar best-fit model parameters of power-law photon index  $\Gamma \simeq 1$  and absorption hydrogen column density  $N_{\text{H}} \simeq 10^{23} \text{ cm}^{-2}$  for all three spectra. The obtained  $N_{\text{H}} \simeq 10^{23} \text{ cm}^{-2}$  is significantly higher than the Galactic hydrogen ( $\text{H}_{\text{I}}$ ) column density in the source direction,  $0.55 \times 10^{22} \text{ cm}^{-2}$  (HI4PI Collaboration

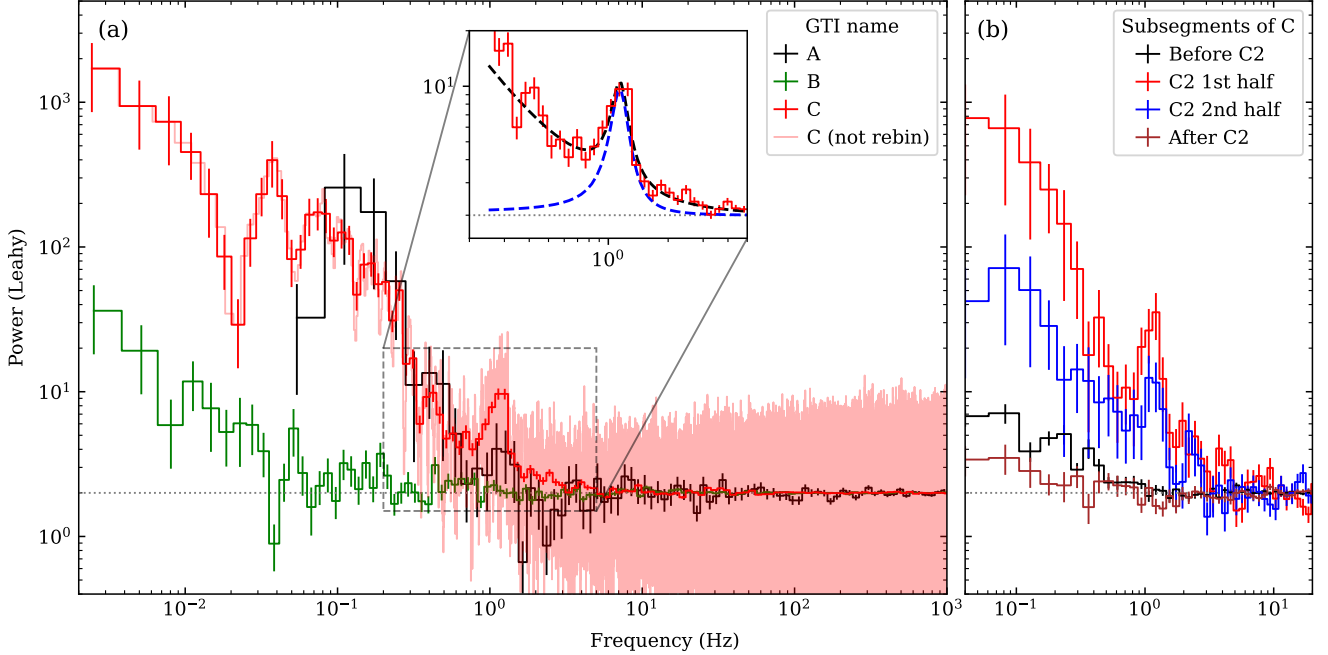


**Figure 4.** (a) Power density spectra (PDS) of NICER 0.5–10 keV light curves in three GTIs, A, B, and C, labeled in figure 1 (middle). The inset shows the close-up view of the peak seen in the PDS of GTI-C at  $\sim 1$  Hz, where dashed lines represent the best-fit Lorentzian plus power-law model in black and its Lorentzian component in blue. (b) PDS of four GTI-C subsegments of before C2 flare, first half and second half of C2, and after C2.

et al. 2016), meaning that the primary X-ray emission from the central X-ray object (presumably NS) is further obscured by local CSM. The goodness of the fits represented by  $W$  for degrees of freedom (d.o.f.) are not within the acceptable level for the two spectra of A and C2\*. The data-to-model residuals show excess remaining in the lower energy band below 1 keV and a possible iron-K $\alpha$  line at 6.4 keV.

We hence modified the simple power-law model by multiplying a partial covering-absorption factor (`tbpcf`) for the local CSM and adding a narrow Gaussian function for the iron-K $\alpha$  line, and then fit it to the data. The modified model is expressed by `tbabs*tbpcf*(powerlaw+gauss)` in XSPEC terminology. There,  $N_{\text{H}}$  for the ISM in the `tbabs` model was fixed at the Galactic  $\text{H}_{\text{I}}$  density  $= 0.55 \times 10^{22} \text{ cm}^{-2}$ , while the partial-covering absorption parameters for the CSM in the `tbpcf` model were allowed to vary. The Gaussian centroid and width for the iron-K $\alpha$  line were fixed at 6.4 keV and 0.1 keV, those typical values in HMXBs (Giménez-García et al. 2015; Pradhan et al. 2018), respectively. Also, the background models were fixed at the default SCORPEON. Then, the fits became acceptable in all three spectra. In figure 5, the best-fit models folded with the instrument response functions and the data-to-model residuals are shown. The uncov-

ered fraction of the partial covering absorber  $1 - f_{\text{pc}}$  is suggested to be significantly  $> 0$  in A and C2\* although as small as  $\sim 10^{-2}$ . The iron-K $\alpha$  line is positively detected only in the C2\* spectrum with a confidence level of 99% or higher.

The systematic excess residuals below 1 keV in the first model fits may be partly due to the errors on the SCORPEON background models. To examine the impact of the background-model errors, we repeated the model fitting by floating the SCORPEON model parameters within their allowed ranges. In figure 5, the best-fit background and emission models are overlaid on those obtained with the default SCORPEON models. The difference is clear in the C2\* spectrum. The predicted background level increased by a factor of  $\sim 5$  and the uncovered fraction of the partial covering absorber  $1 - f_{\text{pc}}$  turned to accept 0. On the other hand, the iron-K $\alpha$  line parameters almost unchanged.

Table 2 lists all the best-fit spectral parameters including power-law photon index  $\Gamma$ , column density of the partial covering absorber  $N_{\text{H,pc}}$ , uncovered fraction  $1 - f_{\text{pc}}$ , iron-K $\alpha$  line flux  $F_{\text{FeK}\alpha}$  and equivalent width  $EW_{\text{FeK}\alpha}$ , model flux with ISM/CSM absorption  $F_{\text{abs}}$ , absorption-corrected flux  $F_{\text{unabs}}$ , and absorption-corrected luminosity  $L_{\text{ubabs}}$  assuming the isotropic source emission at the 3 kpc distance.  $F_{\text{abs}}$ ,

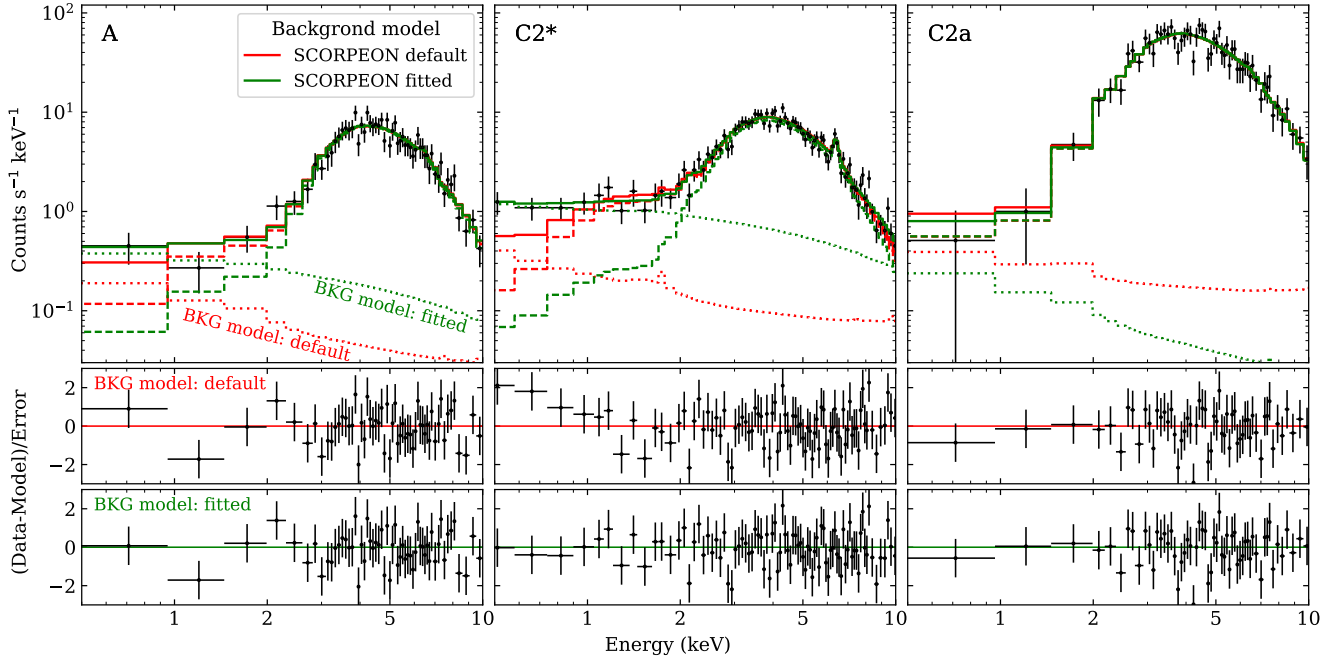


**Figure 5.** X-ray spectra of three flaring periods, A, C2\* (C2 excluding C2a), and C2a, labeled in figure 2. **(Top)** Observed photon count spectra including backgrounds and best-fit models folded with instrument response functions (solid lines). Dashed and dotted lines represent partial-covering-absorption power-law plus iron-K $\alpha$  line models for source spectra and background models with SCORPEON default (red) and those fitted (green). **(Middle and bottom)** Data-to-model residuals with default SCORPEON background models and those allowed to fit in the source model fitting.

$F_{\text{unabs}}$ , and  $L_{\text{ubabs}}$  are calculated in the observed energy band of 0.5–10 keV. There, results obtained with two background models of the default SCORPEON model parameters and those allowed to fit to the data are shown together.

Comparing the obtained model parameters in A with those obtained from the MAXI/GSC data for a possible continuous flare (Sugizaki et al. 2022),  $\Gamma \simeq 1$  in the present NICER results is smaller than  $\Gamma \simeq 2$  in the MAXI data. This is considered from the difference in the energy band between the NICER/XTI 0.5–10 keV and the MAXI/GSC 2–20 keV and suggests that the power-law model should have a break or cutoff at around 10 keV. We hence fitted the MAXI/GSC spectrum in Sugizaki et al. (2022) with an exponential cutoff power-law (`cutoffpl` in Xspec terminology) with  $\Gamma = 1$  and  $N_{\text{H}} = 1.4 \times 10^{23} \text{ cm}^{-2}$  fixed at the present NICER results, and obtained the e-folding energy  $E_{\text{fold}} = 22_{-13}^{+\infty}$  keV. In this cutoff power-law model, the conversion factor from the 0.5–10 keV flux to the bolometric flux is  $\sim 2.9$ .

We also attempt to fit with a model employing a blackbody continuum in place of the power-law continuum, represented by `tbabs*tbpcf*(bbodyrad+gauss)` in Xspec terminology. The obtained  $W$  for d.o.f. are not as good as those for the power-law continuum model but

close to the acceptable level. The best-fit parameters for each of the three spectra are shown together in Table 2. The blackbody temperature  $kT_{\text{BB}} \sim 2$  keV is consistent with that of the MAXI/GSC results in the same flare period (Sugizaki et al. 2022).

#### 4. DISCUSSIONS

MAXI J0709 is a new X-ray transient discovered on 2022 January 25. The transient outburst behavior characterized by the short duration of a few hours, rapid variability with a time scale of  $\lesssim 1$  s, and large luminosity swing from  $10^{32} \text{ erg s}^{-1}$  to  $10^{37} \text{ erg s}^{-1}$  agree with that of the typical SFXTs (Sugizaki et al. 2022). The heavy X-ray absorption of  $N_{\text{H}} \sim 10^{22} - 10^{23} \text{ cm}^{-2}$  changing during the short outburst period is not typical but similar spectral changes has been reported for a few SFXTs (e.g. Bozzo et al. 2011). On the other hand, the optical companion, LY CMA, exhibits properties of both a Be star as well as a B supergiant. Therefore, the mechanism of mass accretion onto the compact object, which is presumably a magnetized NS, has been under debate (Sugizaki et al. 2022). The results of the NICER data analysis in the previous section reveal the extreme variability feature in more detail. We here consider possible mechanisms that can explain all of the observed results.



**Table 2.** Best-fit spectral parameters of partial-covering-absorption power-law or blackbody model for three flaring periods A, C2\* (C2 excluding C2a), and C2a with default or fitted SCORPEON background model.

Flare ID name	A	C2*	C2a	A	C2*	C2a
Background model	SCORPEON default			SCORPEON fitted		
Spectral model	$a_{\text{tbabs}}*_{\text{tbpcf}}*(\text{powerlaw}+\text{gauss})$					
$N_{\text{H,pc}}$ ( $10^{22}$ cm $^{-2}$ ) <sup>b</sup>	14.0 $^{+2.5}_{-2.4}$	10.2 $^{+1.0}_{-1.0}$	7.9 $^{+1.4}_{-1.2}$	14.3 $^{+2.7}_{-2.5}$	11.3 $^{+1.4}_{-1.3}$	7.8 $^{+1.4}_{-1.2}$
$1 - f_{\text{pc}}$ ( $10^{-2}$ )	0.42 $^{+0.41}_{-0.24}$	1.15 $^{+0.44}_{-0.33}$	< 0.32	0.24 $^{+0.34}_{-0.22}$	< 0.28	< 0.36
$\Gamma$	1.07 $^{+0.36}_{-0.35}$	1.32 $^{+0.20}_{-0.20}$	0.83 $^{+0.30}_{-0.29}$	1.12 $^{+0.38}_{-0.37}$	1.62 $^{+0.26}_{-0.25}$	0.80 $^{+0.30}_{-0.29}$
$N_{\text{PL}}$ (photons cm $^{-2}$ s $^{-1}$ at 1 keV)	0.11 $^{+0.11}_{-0.05}$	0.14 $^{+0.06}_{-0.04}$	0.44 $^{+0.32}_{-0.18}$	0.12 $^{+0.13}_{-0.06}$	0.22 $^{+0.14}_{-0.08}$	0.42 $^{+0.30}_{-0.17}$
$F_{\text{FeK}\alpha}$ ( $10^{-11}$ erg cm $^{-2}$ s $^{-1}$ ) <sup>c</sup>	< 2.4	2.2 $^{+1.1}_{-1.0}$	< 13.3	< 2.5	2.4 $^{+1.1}_{-1.0}$	< 13.1
$EW_{\text{FeK}\alpha}$ (eV) <sup>c</sup>	< 155	173 $^{+99}_{-70}$	< 138	< 183	212 $^{+115}_{-85}$	< 112
$F_{\text{abs}}$ ( $10^{-9}$ erg cm $^{-2}$ s $^{-1}$ ) <sup>d</sup>	0.71 $^{+0.06}_{-0.06}$	0.66 $^{+0.03}_{-0.03}$	5.23 $^{+0.45}_{-0.45}$	0.69 $^{+0.06}_{-0.06}$	0.56 $^{+0.03}_{-0.03}$	5.28 $^{+0.46}_{-0.44}$
$F_{\text{unabs}}$ ( $10^{-9}$ erg cm $^{-2}$ s $^{-1}$ ) <sup>d</sup>	1.54 $^{+0.40}_{-0.24}$	1.42 $^{+0.20}_{-0.14}$	8.48 $^{+1.23}_{-0.72}$	1.56 $^{+0.45}_{-0.26}$	1.54 $^{+0.38}_{-0.24}$	8.49 $^{+1.12}_{-0.73}$
$L_{\text{unabs}}$ ( $10^{36}$ erg s $^{-1}$ ) <sup>e</sup>	1.69 $^{+0.44}_{-0.26}$	1.56 $^{+0.21}_{-0.16}$	9.31 $^{+1.35}_{-0.79}$	1.71 $^{+0.50}_{-0.29}$	1.69 $^{+0.42}_{-0.27}$	9.33 $^{+1.23}_{-0.80}$
W/d.o.f.	68.3 / 81	99.8 / 95	74.7 / 81	67.9 / 77	79.3 / 91	74.5 / 77
Spectral model	$a_{\text{tbabs}}*_{\text{tbpcf}}*(\text{bbodyrad}+\text{gauss})$					
$N_{\text{H,pc}}$ ( $10^{22}$ cm $^{-2}$ ) <sup>b</sup>	10.4 $^{+2.3}_{-2.0}$	6.8 $^{+0.9}_{-0.9}$	5.4 $^{+0.9}_{-0.8}$	10.5 $^{+2.3}_{-1.9}$	7.8 $^{+1.0}_{-0.9}$	5.4 $^{+0.9}_{-0.8}$
$1 - f_{\text{pc}}$ ( $10^{-2}$ )	1.79 $^{+1.41}_{-1.17}$	6.44 $^{+1.78}_{-1.51}$	< 1.17	< 1.59	< 0.87	< 1.21
$T_{\text{BB}}$ (keV)	2.27 $^{+0.38}_{-0.29}$	2.05 $^{+0.17}_{-0.15}$	2.38 $^{+0.36}_{-0.28}$	2.18 $^{+0.37}_{-0.28}$	1.61 $^{+0.14}_{-0.12}$	2.39 $^{+0.36}_{-0.28}$
$R_{\text{BB}}$ (km)	0.71 $^{+0.18}_{-0.15}$	0.76 $^{+0.10}_{-0.09}$	1.67 $^{+0.33}_{-0.28}$	0.75 $^{+0.20}_{-0.16}$	1.05 $^{+0.18}_{-0.15}$	1.65 $^{+0.33}_{-0.28}$
$F_{\text{FeK}\alpha}$ ( $10^{-11}$ erg cm $^{-2}$ s $^{-1}$ ) <sup>c</sup>	< 2.0	1.7 $^{+1.0}_{-0.9}$	< 10.7	< 2.1	2.3 $^{+1.0}_{-0.9}$	< 10.6
$EW_{\text{FeK}\alpha}$ (eV) <sup>c</sup>	< 145	138 $^{+78}_{-75}$	< 123	< 152	228 $^{+132}_{-83}$	< 116
$F_{\text{abs}}$ ( $10^{-9}$ erg cm $^{-2}$ s $^{-1}$ ) <sup>d</sup>	0.69 $^{+0.06}_{-0.06}$	0.65 $^{+0.04}_{-0.03}$	5.06 $^{+0.47}_{-0.43}$	0.65 $^{+0.06}_{-0.06}$	0.49 $^{+0.03}_{-0.03}$	5.09 $^{+0.46}_{-0.42}$
$F_{\text{unabs}}$ ( $10^{-9}$ erg cm $^{-2}$ s $^{-1}$ ) <sup>d</sup>	1.05 $^{+0.10}_{-0.09}$	0.89 $^{+0.05}_{-0.04}$	6.58 $^{+0.56}_{-0.48}$	1.02 $^{+0.11}_{-0.05}$	0.78 $^{+0.05}_{-0.04}$	6.60 $^{+0.55}_{-0.48}$
$L_{\text{unabs}}$ ( $10^{36}$ erg s $^{-1}$ ) <sup>e</sup>	1.16 $^{+0.11}_{-0.10}$	0.98 $^{+0.05}_{-0.05}$	7.23 $^{+0.62}_{-0.52}$	1.12 $^{+0.12}_{-0.06}$	0.85 $^{+0.06}_{-0.04}$	7.25 $^{+0.61}_{-0.52}$
W/d.o.f.	68.6 / 81	144.0 / 95	78.3 / 81	67.3 / 77	81.9 / 91	78.3 / 77

<sup>a</sup>  $N_{\text{H}}$  of **tbabs** model for ISM is fixed at the Galactic  $\text{H}_{\text{I}}$  density ( $= 0.55 \times 10^{22} \text{ cm}^{-2}$ ).<sup>b</sup>  $N_{\text{H}}$  of **tbpcf** model for partial covering absorber<sup>c</sup> Flux ( $F_{\text{FeK}\alpha}$ ) and equivalent width ( $EW_{\text{FeK}\alpha}$ ) of iron-K $\alpha$  6.4 keV line modeled with a narrow ( $\sigma = 0.1 \text{ keV}$ ) Gaussian<sup>d</sup> Absorbed ( $F_{\text{abs}}$ ) or unabsorbed ( $F_{\text{unabs}}$ ) 0.5-10 keV flux<sup>e</sup> Unabsorbed 0.5-10 keV lminosity assuming isotropic emission located at 3 kpc distance

#### 4.1. Short-duration rapid-flaring activity

The NICER light curves in figures 1 and 2 reveal that the X-ray flare activity continued to appear until  $t \sim 7$  h from the first MAXI/GSC detection at  $t = 0$ , but its duty cycle is limited to a few short segments including the three remarkable flare periods of A:  $\sim 50$  s, C1:  $\sim 50$  s, and C2:  $\sim 100$  s (see figure 2). Since the total NICER exposure from the observation start at  $t = 3$  h to 7 h is 3269 s, the flare duty cycle during this 4 hours is  $\sim (50 + 50 + 100\text{s})/3269\text{s} \simeq 0.06$ . The duty cycle of the initial 3 hours from  $t = 0$  to 3 h covered by the MAXI/GSC survey is roughly estimated to be  $\sim 0.5$  from the significant X-ray detections at the first ( $t = 0$ ) and third ( $t \simeq 3$  h) scans and the non-detection at the

second scan ( $t \simeq 1.5$  h). Therefore, the duty cycle of the flare activity during the entire 7-h outburst period,  $\delta_{\text{fl}}$ , can be roughly estimated as

$$\delta_{\text{fl}} \sim \frac{0.5 \times 3 + 0.06 \times 4}{7} \simeq 0.25. \quad (1)$$

The overall outburst profile consisting of very sparse, short-lived ( $\lesssim 100$  s), flaring periods seems even extreme compared to those of other typical SFXE outbursts (e.g. Romano et al. 2013; Bozzo et al. 2017). The fine light-curve profile in figure 2 shows that each flare consists of short spikes, each lasting a few seconds and reaching typically  $\sim 100 \text{ cts s}^{-1}$  at the peak. Assuming the spectral model of a cutoff power-law continuum of  $\Gamma \simeq 1$  and  $E_{\text{fold}} = 22 \text{ keV}$  obtained in section 3.4, the count rate

$\sim 100 \text{ cts s}^{-1}$  corresponds to the absorption-corrected bolometric luminosity of  $\sim 1.8 \times 10^{37} \text{ erg s}^{-1}$ . Therefore, the maximum count rate of  $1000 \text{ cts s}^{-1}$  in the data of every 0.1-s time bin indicates that the source luminosity reached up to  $\sim 1.8 \times 10^{38} \text{ erg s}^{-1}$  during the peak 0.1 seconds. It is almost equal to the Eddington limit for a typical  $1.4M_{\odot}$  NS and comparable to those of the brightest SFXTs that have ever been reported (e.g. Bozzo et al. 2015; Romano et al. 2015).

#### 4.2. Local absorption medium and iron-K $\alpha$ line

In the X-ray spectral analysis in section 3.4, we found that each flare spectrum is represented by a power-law of  $\Gamma \simeq 1$  with a heavy partial-covering absorption of  $N_{\text{H,pc}} = (8\sim 14) \times 10^{22} \text{ cm}^{-2}$  and  $1 - f_{\text{pc}} \lesssim 0.02$ . The 6.4 keV iron-K $\alpha$  line, suggesting the emission from neutral iron, with  $EW_{\text{FeK}\alpha} \simeq 100 \text{ eV}$  was detected in the C2\* spectrum, which is collected from the flare C2 except for the brightest 4 s (designated C2a). These power-law model and iron-K $\alpha$  line parameters agree well with those of other HMXBs including SFXTs (e.g. Pradhan et al. 2018). The  $EW_{\text{FeK}\alpha}$  to  $N_{\text{H,pc}}$  ratio  $\sim 100 \text{ eV} / 10^{23} \text{ cm}^{-2}$  suggests that the CSM distribution around the primary X-ray source is not completely uniform, in which case the ratio should be  $\simeq 30 \text{ eV} / 10^{23} \text{ cm}^{-2}$  (Inoue 1985; Torrejón et al. 2010). The discrepancy between  $\Gamma \sim 1$  obtained here and  $\Gamma \sim 2$  obtained from the MAXI spectrum for a possible continuous flare (Sugizaki et al. 2022) suggests a cutoff or break in the simple power-law model at  $\sim 10 \text{ keV}$ . We fitted the MAXI spectrum with an exponential cutoff power-law model and obtained the best-fit  $E_{\text{fold}} = 22^{+8}_{-13} \text{ keV}$ , which is consistent with that in typical HMXBs (e.g. Makishima et al. 1999; Coburn et al. 2002).

Figure 6 shows the changes in the obtained best-fit parameters of the partial-covering-absorption power-law model,  $F_{\text{unabs}}$ ,  $N_{\text{H,pc}}$ ,  $1 - f_{\text{pc}}$ ,  $\Gamma$ , and  $EW_{\text{FeK}\alpha}$  among the three flare periods of A, C2\*, and C2a in table 2.  $N_{\text{H,pc}}$  decreased from the flare A to C2\* and C2a, consistent with the hardness-ratio decrease from A to C2\* and C2a in figure 3. During the flare C2,  $F_{\text{unabs}}$  increased from C2\* to C2a, while all other parameters,  $N_{\text{H,pc}}$ ,  $1 - f_{\text{pc}}$ ,  $\Gamma$ , and  $EW_{\text{FeK}\alpha}$ , apparently decreased. If the SCORPEON background model parameters are allowed to vary from the default model values, the change in  $1 - f_{\text{pc}}$  becomes insignificant but the changes in  $N_{\text{H,pc}}$ ,  $\Gamma$ , and  $EW_{\text{FeK}\alpha}$  become more significant. We estimated the significance of these  $N_{\text{H,pc}}$ ,  $\Gamma$ , and  $EW_{\text{FeK}\alpha}$  changes to be greater than 95%, 95%, and 90%, respectively, by  $\chi^2$  tests, for both background models of the default SCORPEON parameters and those fitted within the allowed parameter ranges.

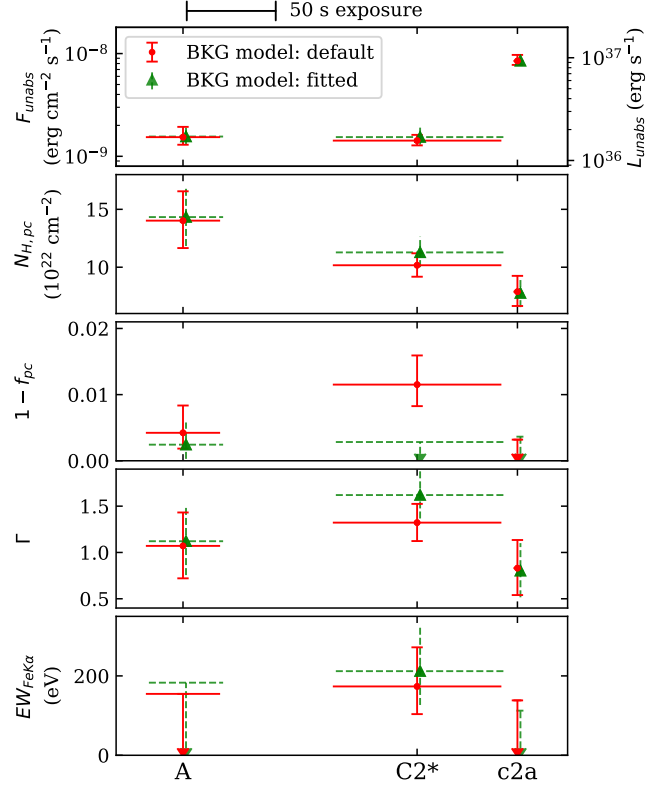


**Figure 6.** Best-fit spectral parameters,  $F_{\text{unabs}}$  ( $L_{\text{unabs}}$ ),  $\Gamma$ ,  $N_{\text{H,pc}}$ ,  $1 - f_{\text{pc}}$ , and  $EW_{\text{FeK}\alpha}$  of a power-law continuum model for three flaring periods, A, C2\*, and C2a, listed in table 2, assuming background models of SCORPEON default (red) and that fitted (green) shown in figure 5. The vertical error bars represent the 90% confidence limits of the statistical uncertainties. The length of horizontal bars represents the exposure time of each data in a scale given at the top.

The  $N_{\text{H,pc}}$  and  $EW_{\text{FeK}\alpha}$  give us information on the CSM distribution around the primary X-ray source. The anti-correlations between  $F_{\text{unabs}}$  and  $EW_{\text{FeK}\alpha}$  can be naturally explained by a scenario that the primary X-ray emission from the compact X-ray object is anisotropic and the beamed emission direction was aligned to the line of sight at the time of the flare peak (C2a), where the relative intensity of the direct component dominating the continuum spectrum increased but that of the reprocess component by the surrounding CSM, which is a major source of iron-K $\alpha$  emission line, decreased. In figure 7, the overall schematic picture is illustrated. Although, alternative scenarios cannot be ruled out.

#### 4.3. Application to clumpy wind accretion model

The outburst light curve discussed above, characterized by short, sparse, rapid-flaring activity, is different from that of typical BeXBs (e.g. Reig 2011) and leads us

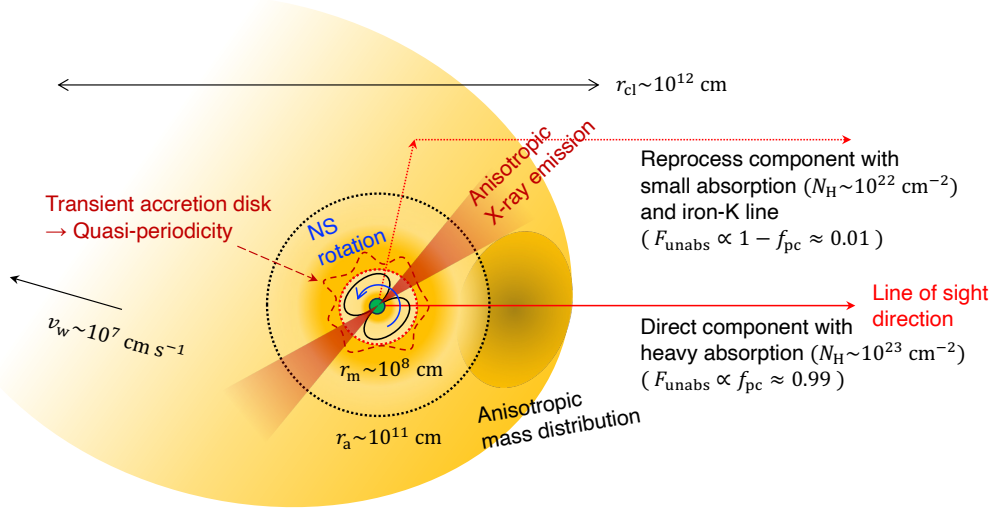


**Figure 7.** Schematic picture of compact X-ray object and surrounding CSM distribution suspected from X-ray spectral changes and rapid flaring activities during the short outburst based on the clumpy wind accretion scenario.

to the idea of mass accretion via clumpy stellar winds that has been considered for SgXBs (e.g. Bozzo et al. 2016a). In fact, the outburst duration of  $\sim 7$  h ( $= 2 \times 10^4$  s) and spectral variation due to  $N_H$  change from  $10^{22}$  to  $10^{23}$   $\text{cm}^{-2}$  are quite similar to those observed previously in a typical SFXT, IGR J18410–0535 (Bozzo et al. 2011), although the peak luminosity ( $\gtrsim 10^{37}$   $\text{erg s}^{-1}$ ) is significantly higher than in the IGR J18410–0535 case ( $\sim 10^{35}$   $\text{erg s}^{-1}$ ). Hence, following the previous SFXT example, we examine the present results with a wind-accretion scenario that has not been considered for BeXBs. We denote the mass and radius of the compact X-ray object, which is likely to be a NS, by  $M_{\text{NS}}$  and  $R_{\text{NS}}$ , and those of the mass-donating stellar companion LY CMa by  $M_*$  and  $R_*$ , hereafter.

The radial extent of the clump  $r_{\text{cl}}$  is roughly estimated from the outburst duration  $t_{\text{ob}}$  and relative velocity  $v_{\text{rel}}$  between the clump and the NS as

$$r_{\text{cl}} \simeq v_{\text{rel}} t_{\text{ob}} = 10^{12} v_{\text{rel}8} t_{\text{ob}4} \text{ cm} \quad (2)$$

where  $t_{\text{ob}4} = t_{\text{ob}}/10^4$  s and  $v_{\text{rel}8} = v_{\text{rel}}/10^8$   $\text{cm s}^{-1}$ . Because the clump moves with the stellar wind, its radial velocity from the donor star LY CMa is approximated by the wind velocity  $v_w$ . Bhattacharyya et al. (2022) derived the effective temperature  $T_{\text{eff}} = 20$  kK and  $R_* \simeq 11.8 R_{\odot} = 8.2 \times 10^{11}$  cm from the optical SED model fit assuming the object to be an evolved Be star with a surface gravity  $\log g = 3$ . These  $R_*$  and  $\log g$  indicate  $M_* = 5 M_{\odot}$ , which agrees with the typical Be-star mass, and the surface escape velocity of  $v_{\text{esc}} = 4.0 \times 10^7$   $\text{cm s}^{-1}$ . The terminal wind velocity  $v_{\infty}$  is then estimated to be  $\sim (4-8) \times 10^7$   $\text{cm s}^{-1}$

from  $v_{\infty}/v_{\text{esc}} \sim 1-2$  in B1.5 Be stars (Prinja 1989) and B supergiants (Crowther et al. 2006), which is slower than  $v_{\infty} \gtrsim 10^8$   $\text{cm s}^{-1}$  in typical SgXBs (Hainich et al. 2020). Meanwhile, the orbital velocity  $v_{\text{orb}}$  of the compact X-ray object around the primary star LY CMa and the distance between the two objects  $r_{\text{orb}}$  are expressed using the orbital parameters, orbital period  $P_{\text{orb}}$  and eccentricity  $e$ , as

$$r_{\text{orb}} = \left\{ \frac{G (M_{\text{NS}} + M_*) P_{\text{orb}}^2}{4\pi^2} \right\}^{1/3} (1 \pm e) \\ = 2.5 \times 10^{12} P_{10\text{d}}^{2/3} M_{6.4}^{1/3} (1 \pm e) \text{ cm}, \quad (3)$$

$$v_{\text{orb}} = \left\{ \frac{2\pi G (M_{\text{NS}} + M_*)}{P_{\text{orb}}} \right\}^{1/3} \frac{\sqrt{1-e^2}}{1 \pm e} \\ = 1.8 \times 10^7 P_{10\text{d}}^{-1/3} M_{6.4}^{1/3} \frac{\sqrt{1-e^2}}{1 \pm e} \text{ cm s}^{-1} \quad (4)$$

where  $P_{10\text{d}} = P_{\text{orb}}/10$  d,  $M_{6.4} = (M_{\text{NS}} + M_*)/(1.4 M_{\odot} + 5 M_{\odot})$ , and the  $\pm$  signs represent equations for periastron (–) and apastron (+) epochs, respectively. Then, assuming the standard wind-velocity law so called  $\beta$ -velocity law

$$v_w = v_{\infty} \left( 1 - \frac{R_*}{r_{\text{orb}}} \right)^{\beta} \quad (5)$$

where  $\beta \sim 0.5$  in a classical line-driven wind model (Castor et al. 1975) has been revised to  $\beta \sim 0.8-2$  with hydrodynamical calculations and observations (e.g. Crowther et al. 2006; Kr̕t̕čka & Kub̕t̕ 2011), we can calculate  $v_w$  from  $v_{\infty}$ ,  $R_*$  and  $r_{\text{orb}}$  estimated above and the orbital parameters,  $P_{\text{orb}}$  and  $e$ , which are unknown. Equation (5) means that the larger  $r_{\text{orb}}$  is, the closer  $v_w$

is to  $v_\infty$ . Assuming  $P_{\text{orb}} \simeq 10$  d and  $e \lesssim 0.4$  (not extremely eccentric) as typical in BeXBs (e.g. Kretschmar et al. 2019), we can roughly estimate from equations (3)(4)(5) that  $r_{\text{orb}} \sim 2.5 \times 10^{12}$  cm,  $v_{\text{orb}} \sim 1.8 \times 10^7$  cm s $^{-1}$ , and thus  $v_w \sim 0.5^\beta v_\infty \sim (1-4) \times 10^7$  cm s $^{-1}$ . Therefore, we expect mostly  $v_{\text{orb}} \lesssim v_w$  in typical binary conditions as discussed. Given these expected ranges of  $v_{\text{orb}}$  and  $v_w$ , we can estimate  $v_{\text{rel}} \simeq \sqrt{v_{\text{orb}}^2 + v_w^2}$  to be  $\sim (2.5-6) \times 10^7$  cm s $^{-1}$ .

When the NS enters the clump, the matter within the accretion radius  $r_a$ ,

$$\begin{aligned} r_a &= 2GM_{\text{NS}}/v_{\text{rel}}^2 \\ &= 3.7 \times 10^{10} M_{1.4} v_{\text{rel}8}^{-2} \text{ cm} \end{aligned} \quad (6)$$

is accreted (Bondi 1952). Assuming that the mass distribution in the clump is approximately uniform, the relation between the total clump mass  $M_{\text{cl}}$  and the accretion mass  $M_{\text{acc}}$  is given by

$$M_{\text{cl}} = (r_{\text{cl}}/r_a)^2 M_{\text{acc}}. \quad (7)$$

Meanwhile,  $M_{\text{acc}}$  can be estimated from the outburst light curve representing the luminosity  $L(t)$  as a function of time  $t$  by assuming that the X-ray emission is powered by mass accretion onto the NS surface, i.e.

$$GM_{\text{NS}}M_{\text{acc}}/R_{\text{NS}} = \int L(t)dt = L_{\text{fl}}\delta_{\text{fl}}t_{\text{ob}} \quad (8)$$

where  $L_{\text{fl}}$  is the average luminosity during the flaring duty cycle ( $= \delta_{\text{fl}}t_{\text{ob}}$ ) out of the entire outburst period, i.e.  $L_{\text{fl}} \sim 10^{36}$  erg s $^{-1}$ . From equations (2)(6)(7)(8), we obtain

$$\begin{aligned} M_{\text{cl}} &= \frac{R_{\text{NS}}L_{\text{fl}}\delta_{\text{fl}}t_{\text{ob}}^3v_{\text{rel}}^6}{(GM_{\text{NS}})^3} \\ &\simeq 1.6 \times 10^{22} M_{1.4}^{-3} R_6 L_{36} \delta_{0.1} t_{\text{ob}4}^3 v_{\text{rel}8}^6 \text{ g}, \end{aligned} \quad (9)$$

where  $L_{36} = L_{\text{fl}}/10^{36}$  erg s $^{-1}$  and  $\delta_{0.1} = \delta_{\text{fl}}/0.1$ . Then, the hydrogen column density through the clump  $N_{\text{H,cl}}$  is represented by

$$\begin{aligned} N_{\text{H,cl}} &= \frac{M_{\text{cl}}}{r_{\text{cl}}^2 m_p} = \frac{R_{\text{NS}}L_{\text{fl}}\delta_{\text{fl}}t_{\text{ob}}^4v_{\text{rel}}^4}{(GM_{\text{NS}})^3} \\ &\simeq 0.9 \times 10^{22} M_{1.4}^{-3} R_6 L_{36} \delta_{0.1} t_{\text{ob}4}^4 v_{\text{rel}8}^4 \text{ cm}^{-2}, \end{aligned} \quad (10)$$

where  $m_p$  is the proton mass. Applying the observed parameters,  $L_{36} \sim 5$ ,  $\delta_{0.1} \sim 2.5$ , and  $t_{\text{ob}4} \sim 2$  obtained from the present data analysis, and  $v_{\text{rel}8} \sim 0.25-0.6$  estimated above into the equations (9) and (10), we obtain  $M_{\text{cl}} \sim (0.04-7) \times 10^{22}$  g and  $N_{\text{H,cl}} \sim (0.09-3) \times 10^{22}$  cm $^{-2}$ . The calculated  $N_{\text{H,cl}}$  is smaller than the absorption column density  $N_{\text{H,pc}} \sim 1 \times 10^{23}$  cm $^{-2}$  for the X-ray

source determined by the spectral analysis (section 3.4). On the other hand, the  $M_{\text{cl}} \sim 10^{22}$  g is on the larger side among those of typical SgXBs, which are  $\sim 10^{18}$  to  $10^{22}$  g (e.g. Martínez-Núñez et al. 2017). These discrepancies suggest that the clump mass distribution is not spherically uniform as assumed in equation (7), but may be like a filament or a cluster of multiple clumps.

In figure 7, the scales of  $r_{\text{cl}} \sim 10^{12}$  cm and  $r_a \sim 10^{11}$  cm are schematically presented.

#### 4.4. Quasi-periodic variation and transient accretion-disk scenario

The PDS in figure 4 reveals characteristic structures below  $\sim 0.5$  Hz during the flare activities and also an isolated peak at 1.1 Hz during the brightest flare of  $L \simeq 10^{37}$  erg s $^{-1}$ . Because the PDS peak has a width typical of QPOs, it is unlikely to be a coherent pulsation due to the NS spin. What does the QPO represent?

QPOs have been reported in a number of HMXB pulsars, mostly BeXB pulsars (e.g. Angelini et al. 1989; Takeshima et al. 1994; Finger et al. 1996; James et al. 2010; Devasia et al. 2011; Roy et al. 2019; Pike et al. 2023) but also a few SgXB pulsars (e.g. Rikame et al. 2022; Liu et al. 2022). In these HMXB pulsars, QPOs appeared at frequencies from 1 mHz to 1.2 Hz (James et al. 2010). The present QPO peak of 1.1 Hz is close to the highest one of 1.2 Hz observed in XTE J0111.2-7317 (Kaur et al. 2007). The periodicities of the QPOs in the HMXB pulsars have been considered mainly from the Keplerian rotation frequency at the inner edge of the accretion disk interacting with the NS magnetosphere (Keplerian Frequency Model; KFM; van der Klis et al. 1987) or its beat frequency with the NS spin frequency (Beat Frequency Model; BFM; Alpar & Shaham 1985). These models successfully explain some of the QPOs observed in BeXBs (e.g. Finger et al. 1996), but the attempt to explain all of these features with a unified picture has not been successful (Bozzo et al. 2009). The discrepancy between the observed QPO frequencies and those predicted by KFM or BFM assuming the NS magnetic fields measured with the cyclotron resonance features suggests that the QPO model predictions should have an error of about one order of magnitude (e.g. James et al. 2010).

Possible QPOs have been also reported in a few SFXTs. IGR J17544-2619 showed a broad PDS peak at 86 mHz (period = 11.6 s) with the quality factor  $Q \simeq 3$  like QPO during the bright flare of the peak luminosity  $\sim 3 \times 10^{38}$  erg s $^{-1}$  on 2014 October 10 (Romano et al. 2015), but its periodicity has never been confirmed in the later observations (Bozzo et al. 2016b). Also, IGR J19140+0951, a possible intermediate HMXB clas-



sified between classical persistent SgXBs and SFXTs, has shown transient QPOs at 1.46 mHz and 0.17 mHz, the latter of which is considered to represent the NS spin (Sidoli et al. 2016). These irreproducible observation results suggest that their origins would be irregular transient events, such as transient accretion-disk formation (Romano et al. 2015; Sidoli et al. 2016).

We here consider the transient accretion-disk scenario in which QPOs are expected by the KFM or BFM mechanism, following the previous examples mentioned above. As discussed in section 4.3, the wind velocity of LY CMa is expected to be slower than that of typical SgXBs, suggesting a higher mass-capture rate ( $r_a^2 v_{\text{rel}} \propto v_{\text{rel}}^{-3}$ ) that would favor the accretion-disk formation (e.g. Ducci et al. 2010). Assuming that the captured accreting matter conserves its angular momentum as it falls onto the magnetized NS, sustained accretion-disk formation outside the NS magnetosphere requires  $v_{\text{rel}} \lesssim 3.5 \times 10^7 \text{ cm s}^{-1}$  (Wang 1981) under a typical binary orbit introduced at equation (3), which corresponds to the lower end of the estimated possible range  $v_{\text{ref}} \simeq (2.5\text{--}6) \times 10^7 \text{ cm s}^{-1}$  in section 4.3. On the other hand, transient disk formation has been proposed for flare-like events observed in the typical SgXB Vela X-1 with  $v_{\text{ref}} \gtrsim 10^8 \text{ cm s}^{-1}$ , where the inhomogeneous wind density and velocity induce the instability leading to the disk formation and dissipation (Kreykenbohm et al. 2008). In fact, the observed outburst duration  $t_{\text{ob}} \sim 10^4 \text{ s}$  is on the same order of magnitude as the model prediction  $\sim 6GM_{\text{NS}}v_{\text{rel}}^{-3}$  (Taam et al. 1988). Therefore, the transient disk formation scenario is considered to be possible for any  $v_{\text{ref}}$  within the expected range.

The radius  $r_K$  around the NS with a Keplerian orbital frequency  $\nu_K$  is given by

$$r_K = \left( \frac{GM_{\text{NS}}}{4\pi^2 \nu_K^2} \right)^{1/3} = 1.7 \times 10^8 M_{1.4}^{1/3} \nu_K^{-2/3} \text{ cm}. \quad (11)$$

In KFM, the QPO frequency  $\nu_{\text{qpo}} = 1.1 \text{ Hz}$  is expected to be equal to  $\nu_K$  at the inner-disk radius, where the NS spin frequency  $\nu_s$  should be  $< \nu_K = 1.1 \text{ Hz}$  because the mass accretion was not inhibited by centrifugal barrier (propeller effect). In BFM,  $\nu_{\text{qpo}}$  represents the beat frequency between the  $\nu_K$  and  $\nu_s$ , i.e.  $\nu_{\text{qpo}} = \nu_K - \nu_s$ . The  $\nu_s$  has not been known in the present data. The PDS in figure 4 shows no significant coherent pulsation in the 2.5 mHz – 1 kHz range. Considering that most of the HMXB pulsars that have been observed have spin periods  $P_s \gtrsim 1 \text{ s}$ , (e.g. Kretschmar et al. 2019), we can expect likely  $\nu_s \lesssim 1 \text{ Hz}$ , and thus  $\nu_K = \nu_{\text{qpo}} + \nu_s \sim 1\text{--}2 \text{ Hz}$ . Hence, we here focus on the case of  $\nu_K \sim 1 \text{ Hz}$  at the inner-disk radius. We consider the exception

case of  $\nu_K \gg 1 \text{ Hz}$  in the next section. From equation (11), the inner-disk radius  $r_K$  for  $\nu_K \sim 1 \text{ Hz}$  is estimated to be  $\sim 10^8 \text{ cm}$ , which is much smaller than  $r_a \sim 10^{11} \text{ cm}$  in equation (6), suggesting that the accreting matter flow would become roughly spherically uniform within  $r_a$ . The schematic picture is shown on figure 7.

The magnetospheric radius  $r_m$  at which the pressure of the NS magnetic field balances the ram pressure of the accreting matter is expressed by

$$r_m = \zeta \left( \frac{\mu^4}{2GM_{\text{NS}}\dot{M}_{\text{acc}}^2} \right)^{1/7} \quad (12)$$

where  $\mu$  is the NS magnetic dipole moment and  $\zeta (\sim 1)$  is the geometrical factor of the accreting matter flow;  $\zeta = 1$  in spherical accretion and  $\zeta = 0.52$  in the disk accretion model proposed by Ghosh & Lamb (1979a,b). Assuming that the accreting matter releases all the energy on the NS surface with X-ray radiation, i.e.  $L = GM_{\text{NS}}\dot{M}_{\text{acc}}/R_{\text{NS}}$ , equation (12) is reduced to

$$r_m = 2.7 \times 10^8 \zeta \mu_{30}^{4/7} M_{1.4}^{1/7} R_6^{-2/7} L_{37}^{-2/7} \text{ cm}, \quad (13)$$

where  $\mu_{30} = \mu/10^{30} \text{ G cm}^{-3}$  and  $L_{37} = L/10^{37} \text{ erg s}^{-1}$ . If  $r_K = r_m$  as supposed in both KFM and BFM, we obtain the equation of  $\mu_{30}$  from equations (11) and (13),

$$\mu_{30} = 0.44 \zeta^{-7/4} M_{1.4}^{1/3} R_6^{1/2} L_{37}^{1/2} \nu_K^{-7/6}. \quad (14)$$

Hence, the NS surface magnetic field  $B_s = 10^{12} \mu_{30} R_6^3 \text{ G}$  can be estimated from equation (14). Applying the observed parameters of  $L \sim 10^{37} \text{ erg s}^{-1}$  and  $\nu_K \simeq 1 \text{ Hz}$ , we obtain  $B_s \sim 0.4 \times 10^{12} \text{ G}$  in the spherical accretion case ( $\zeta = 1$ ) and  $\sim 2 \times 10^{12} \text{ G}$  in the disk accretion case ( $\zeta \simeq 0.5$ ). This agrees with the typical  $B_s$  of HMXB pulsars  $(1\text{--}10) \times 10^{12} \text{ G}$  measured by cyclotron resonance features (e.g. Makishima et al. 1999).

#### 4.5. What makes MAXI J0709 different from other HXMB systems?

As discussed above, the observed short outburst duration and fast variability are quite unique compared to those of other well-known HMXBs. The X-ray time variation is considered to reflect the manner of mass accretion via CSM fed by the stellar companion. The optical spectroscopic observations suggest the stellar companion LY CMa has a circumstellar Be disk whose structure changed according to the X-ray activity (Bhattacharyya et al. 2022; Shidatsu et al. 2025). However, the X-ray light curve profile does not agree with those of typical BeXBs, which usually cause outbursts lasting for several weeks to months (e.g. Reig 2011), but resembles those of SFXTs. As discussed in section 4.3, the overall profile is largely explained by a clumpy wind accretion scenario,



which has been often applied to SFXTs. Therefore, we expect that the CSM condition around the compact X-ray object would be more similar to those of the SFXTs. In fact, LY CMa is suggested to be an evolved Be star located between standard Be stars and B supergiants on the color-magnitude diagram (Bhattacharyya et al. 2022). Similar objects that can be classified as intermediate SFXTs have been reported (Rahoui & Chaty 2008; González-Galán et al. 2014).

The very sparse flare activity ( $\delta_{\text{fl}} \sim 0.25$ ) consisting of intermittent, short-lived ( $\lesssim 100$  s), rapid-variability (times scale  $\lesssim 1$  s) intervals during the outburst (figures 1, 2) seems extreme compared to typical SFXT outbursts. As estimated in section 4.3, the wind velocity of LY CMa is thought to be slower than in typical SFXTs, which may have some impact on the accretion process, such as the formation of a transient accretion disk (e.g. Ducci et al. 2010), as discussed in section 4.4. Assuming that the compact object is a magnetized NS and the observed 1.1 Hz QPO during the brightest flare is attributed to the inner boundary of the transient accretion disk interacting with the NS magnetosphere at the radius  $r_m$ , the NS surface magnetic field is estimated to be  $B_s \sim 10^{12}$  G, which agrees with those of typical HMXB pulsars (section 4.4). The X-ray spectral results also agree with those of typical HMXB pulsars, whose X-ray emission is considered to originate from close to the magnetic poles on the NS surface (section 3.4). No cyclotron-resonance features corresponding to the  $B_s$  have been detected in X-ray spectra obtained so far (Sugizaki et al. 2022).

The NS spin frequency  $\nu_s$  has not been observed. Based on the KFM scenario that  $\nu_K = \nu_{\text{qpo}} = 1.1$  Hz at  $r_m$ , we expect  $\nu_s < 1.1$  Hz, i.e. spin period  $P_s \gtrsim 1$  s because the propeller effect did not inhibit mass accretion onto the NS surface. In the BFM scenario, it is possible that  $\nu_s > 1$  Hz as long as  $\nu_K - \nu_s = 1.1$  Hz at  $r_m$ . If  $\nu_s \gg 1$  Hz, i.e. a fast-rotating NS like a millisecond pulsar, the NS magnetic field must be weak ( $B_s \ll 10^{12}$  G), as given by equation (14) for  $\nu_K > \nu_s \gg 1$  Hz at  $r_m$ . This case is unlikely, because the observed X-ray light curve and spectral properties are different from those of X-ray binaries with weakly magnetized fast-rotating NS (e.g. Di Salvo & Sanna 2020). The absence of a coherent pulsation signal in the PDS from 2.5 mHz to 1 kHz (figure 4) may suggest that the NS spin axis is closer to the line of sight or that the  $P_s$  is longer than the individual observation segments ( $\sim 1000$  s).

In the possible condition discussed above, where  $\nu_s < \nu_K = 1.1$  Hz at  $r_m$ , the mass accretion is thought to be in the subsonic propeller regime or subsonic settling regime where the accreting matter is halted by the NS

magnetosphere to form a transient accretion disk, and then intermittently settling down onto the NS surface (e.g. Bozzo et al. 2008; Martínez-Núñez et al. 2017). The mechanism for the intermittent settling remains under debate although some possible mechanisms have been proposed, including Kelvin-Helmholtz instability (Bozzo et al. 2008), radiative or Compton cooling (Shakura et al. 2013), and magnetic reconnection (Shakura et al. 2014). The present data will help to resolve the issue. Also, Bozzo et al. (2008) proposed a hypothesis that SFXTs would appear in HMXBs with strongly-magnetized NSs of  $B_s \sim 10^{13} - 10^{14}$  G like magnetars. This disagrees with the present estimate of  $B_s \sim 10^{12}$  G from the 1.1 Hz QPO assuming the KFM/BFM model, but the hypothesis cannot be completely ruled out if the systematic uncertainty on the estimate using the QPO is considered.

## 5. CONCLUSION

We analyzed data of the NICER observations of the new X-ray transient MAXI J0709–159 discovered on 2022 January 25. The object has been identified as a HMXB with a stellar companion LY CMa, which has a complex spectral type between Be stars and B supergiants. The initial X-ray behavior observed by MAXI agrees well with that of typical SFXTs.

The NICER X-ray light curve from 3 hours to 7 days after the discovery reveals that the X-ray activity continued until 7 hours in sparse short flares, each lasting  $\lesssim 100$  s and reaching up to  $\sim 1 \times 10^{38}$  erg s $^{-1}$  at the instantaneous peak of 0.1 seconds. The X-ray spectrum is represented by a power-law continuum of  $\Gamma \sim 1$ , an iron-K $\alpha$  line at 6.4 keV and a partial covering absorption of  $N_{\text{H,pc}} \sim 10^{23}$  cm $^{-2}$  and  $1 - f_{\text{pc}} \sim 0.01$ , which are typical for HMXBs. The spectral parameters were found to vary for each flare, and also during the brightest flare. These light-curve and spectral feature are in reasonable agreement with those expected from a clumpy wind-accretion scenario as proposed for SgXBs. In addition, the variability PDS shows a broad peak at  $\nu_0 = 1.1$  Hz with a width of  $\Delta \simeq 0.11$  Hz like QPO. If the QPO represents the Keplerian rotation at the inner edge of the accretion disk interacting with the NS magnetosphere or its beat frequency with the NS spin, the NS surface magnetic field  $B_s$  is estimated to be  $\sim 10^{12}$  G, which is consistent with those of other typical HMXB pulsars.

What causes the extreme variability in MAXI J0709 characterized by the sparse short flares and the large peak luminosity during the outburst, which is even extreme in the SFXT subclass, is still unresolved. One plausible scenario is that the compact X-ray object is a (slow-rotating) magnetized NS of  $P_s \gtrsim 1$  s and the mass

accretion onto the NS is in the subsonic propeller regime or settling regime, where accreting matter is halted on the the NS magnetosphere and then intermittently settling down onto the NS surface. Because observations of SFXTs during their active outburst phases are fairly limited, theoretical models for these accretion regimes have not been well established and remain under debate. Further MAXI-NICER coordinated operations as well as new time-domain X-ray missions for capturing this type of fast X-ray transients, such as Einstein-Probe X-ray satellite (Yuan et al. 2022), will help resolve these problem.

## ACKNOWLEDGMENTS

MS acknowledges support from the Chinese Academy of Sciences (CAS) President’s International Fellowship Initiative (PIFI) (grant No. 2020FSM004).

*Facilities:* NICER(XTI), MAXI(GSC)

*Software:* Astropy (Astropy Collaboration et al. 2013, 2018), Matplotlib (Hunter 2007), HEASoft (v6.32.1 NASA High Energy Astrophysics Science Archive Research Center (HEASARC) 2014), Stingray (Huppenkothen et al. 2019a,b), Xspec (v12.13.1 Arnaud 1996),

## APPENDIX

### A. GRID SCAN OBSERVATION

The first  $\sim 30$  minutes of the NICER observation was dedicate to the grid scan covering the entire error region reported by MAXI (Serino et al. 2022) in order to confirm the new X-ray source and determine the position with the better accuracy. In figure 8, time evolutions of the 2–8 keV count rate, and the NICER/XTI pointing direction during the observation are plotted on the left three panels and the count rate map on the scanned sky area is plotted on the right panel. The count rate increased significantly over the background level when the XTI was pointed towards a certain direction (Iwakiri et al. 2022) within a radius of  $\sim 3'$ , which is consistent with the size of the XTI field of view. We defined the good time interval for which the XTI was pointed towards the region within the  $3'$  as shown on the count-rate evolution in figure 8 and used it in selecting target events in the following analysis, as described in section 2. The source position was later refined by the NuSTAR observation and the object was identified to the optical counterpart LY CMA (Sugizaki et al. 2022), as plotted on the count-rate map in figure 8.

## REFERENCES

- Alpar, M. A., & Shaham, J. 1985, *Nature*, 316, 239, doi: [10.1038/316239a0](https://doi.org/10.1038/316239a0)
- Angelini, L., Stella, L., & Parmar, A. N. 1989, *ApJ*, 346, 906, doi: [10.1086/168070](https://doi.org/10.1086/168070)
- Arnaud, K. A. 1996, in *Astronomical Society of the Pacific Conference Series*, Vol. 101, *Astronomical Data Analysis Software and Systems V*, ed. G. H. Jacoby & J. Barnes, 17
- Astropy Collaboration, Robitaille, T. P., Tollerud, E. J., et al. 2013, *A&A*, 558, A33, doi: [10.1051/0004-6361/201322068](https://doi.org/10.1051/0004-6361/201322068)
- Astropy Collaboration, Price-Whelan, A. M., Sipőcz, B. M., et al. 2018, *AJ*, 156, 123, doi: [10.3847/1538-3881/aabc4f](https://doi.org/10.3847/1538-3881/aabc4f)
- Bailer-Jones, C. A. L., Rybizki, J., Fouesneau, M., Demleitner, M., & Andrae, R. 2021, *AJ*, 161, 147, doi: [10.3847/1538-3881/abd806](https://doi.org/10.3847/1538-3881/abd806)
- Belloni, T., Psaltis, D., & van der Klis, M. 2002, *ApJ*, 572, 392, doi: [10.1086/340290](https://doi.org/10.1086/340290)
- Bhattacharya, S., Mathew, B., Banerjee, G., et al. 2024, *Bulletin de la Societe Royale des Sciences de Liege*, 93, 636, doi: [10.25518/0037-9565.11821](https://doi.org/10.25518/0037-9565.11821)
- Bhattacharyya, S., Mathew, B., Ezhikode, S. H., et al. 2022, *ApJL*, 933, L34, doi: [10.3847/2041-8213/ac7b8a](https://doi.org/10.3847/2041-8213/ac7b8a)
- Bondi, H. 1952, *MNRAS*, 112, 195, doi: [10.1093/mnras/112.2.195](https://doi.org/10.1093/mnras/112.2.195)
- Bozzo, E., Bernardini, F., Ferrigno, C., et al. 2017, *A&A*, 608, A128, doi: [10.1051/0004-6361/201730398](https://doi.org/10.1051/0004-6361/201730398)
- Bozzo, E., Falanga, M., & Stella, L. 2008, *ApJ*, 683, 1031, doi: [10.1086/589990](https://doi.org/10.1086/589990)
- Bozzo, E., Oskinova, L., Feldmeier, A., & Falanga, M. 2016a, *A&A*, 589, A102, doi: [10.1051/0004-6361/201628341](https://doi.org/10.1051/0004-6361/201628341)
- Bozzo, E., Romano, P., Ducci, L., Bernardini, F., & Falanga, M. 2015, *Advances in Space Research*, 55, 1255, doi: [10.1016/j.asr.2014.11.012](https://doi.org/10.1016/j.asr.2014.11.012)
- Bozzo, E., Stella, L., Vietri, M., & Ghosh, P. 2009, *A&A*, 493, 809, doi: [10.1051/0004-6361:200810658](https://doi.org/10.1051/0004-6361:200810658)

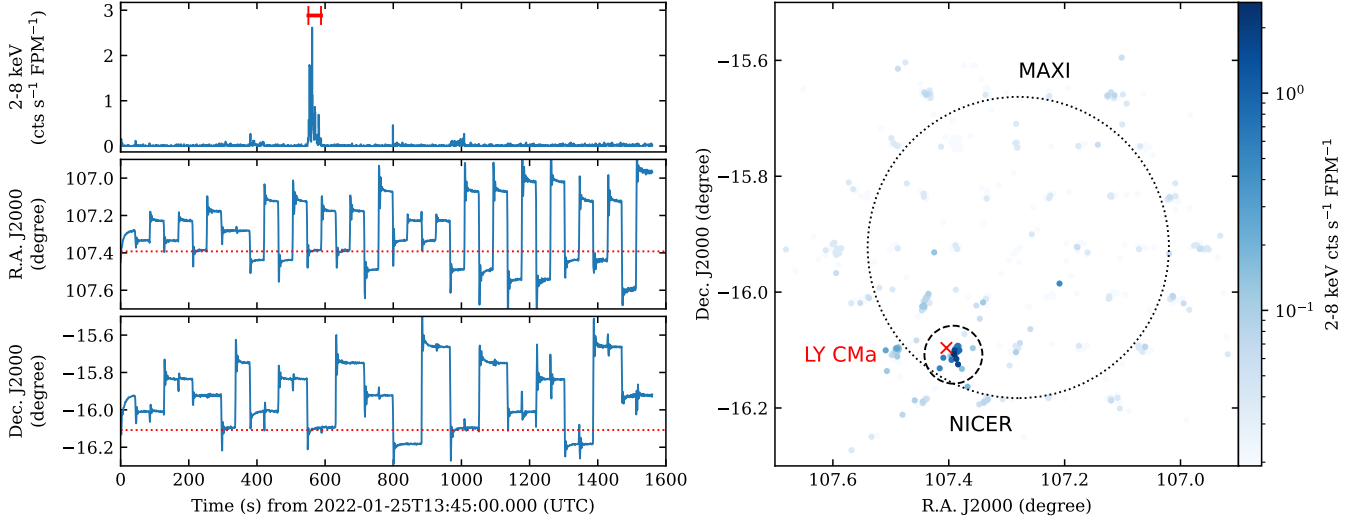


**Figure 8.** (Left) Time evolutions of NICER 2-8 keV count rate (top), J2000 right ascension (middle) and declination (bottom) of the XTI pointing direction during the grid scan of the MAXI J0709 position-error region determined by MAXI. In the top panel, the good time interval determined from the pointing direction is presented in a red line. In the middle and bottom panels, dotted lines correspond to the refined target coordinates. (Right) Count-rate map in the scanned region. A dotted line represents the error circle of a  $0^{\circ}.26$  radius (systematic  $\simeq 0^{\circ}.1$  plus statistic  $\simeq 0^{\circ}.16$ ) given by MAXI. A dashed line represents the NICER error circle of a  $3'$  radius. The data within the NICER circle was used in the source analysis in section 3. A red-cross mark indicates the position of the optical counterpart, LY Cma, identified by the NuSTAR observation.

- Bozzo, E., Giunta, A., Cusumano, G., et al. 2011, *A&A*, 531, A130, doi: [10.1051/0004-6361/201116726](https://doi.org/10.1051/0004-6361/201116726)
- Bozzo, E., Bhalerao, V., Pradhan, P., et al. 2016b, *A&A*, 596, A16, doi: [10.1051/0004-6361/201629311](https://doi.org/10.1051/0004-6361/201629311)
- Cash, W. 1979, *ApJ*, 228, 939, doi: [10.1086/156922](https://doi.org/10.1086/156922)
- Castor, J. I., Abbott, D. C., & Klein, R. I. 1975, *ApJ*, 195, 157, doi: [10.1086/153315](https://doi.org/10.1086/153315)
- Chojnowski, S. D., Whelan, D. G., Wisniewski, J. P., et al. 2015, *AJ*, 149, 7, doi: [10.1088/0004-6256/149/1/7](https://doi.org/10.1088/0004-6256/149/1/7)
- Coburn, W., Heindl, W. A., Rothschild, R. E., et al. 2002, *ApJ*, 580, 394, doi: [10.1086/343033](https://doi.org/10.1086/343033)
- Crowther, P. A., Lennon, D. J., & Walborn, N. R. 2006, *A&A*, 446, 279, doi: [10.1051/0004-6361:20053685](https://doi.org/10.1051/0004-6361:20053685)
- Devasia, J., James, M., Paul, B., & Indulekha, K. 2011, *MNRAS*, 417, 348, doi: [10.1111/j.1365-2966.2011.19269.x](https://doi.org/10.1111/j.1365-2966.2011.19269.x)
- Di Salvo, T., & Sanna, A. 2020, arXiv e-prints, arXiv:2010.09005, doi: [10.48550/arXiv.2010.09005](https://doi.org/10.48550/arXiv.2010.09005)
- Ducci, L., Sidoli, L., & Paizis, A. 2010, *MNRAS*, 408, 1540, doi: [10.1111/j.1365-2966.2010.17216.x](https://doi.org/10.1111/j.1365-2966.2010.17216.x)
- Finger, M. H., Wilson, R. B., & Harmon, B. A. 1996, *ApJ*, 459, 288, doi: [10.1086/176892](https://doi.org/10.1086/176892)
- Gendreau, K. C., Arzoumanian, Z., Adkins, P. W., et al. 2016, in *Society of Photo-Optical Instrumentation Engineers (SPIE) Conference Series*, Vol. 9905, Space Telescopes and Instrumentation 2016: Ultraviolet to Gamma Ray, ed. J.-W. A. den Herder, T. Takahashi, & M. Bautz, 99051H, doi: [10.1117/12.2231304](https://doi.org/10.1117/12.2231304)
- Ghosh, P., & Lamb, F. K. 1979a, *ApJ*, 232, 259, doi: [10.1086/157285](https://doi.org/10.1086/157285)
- . 1979b, *ApJ*, 234, 296, doi: [10.1086/157498](https://doi.org/10.1086/157498)
- Giménez-García, A., Torrejón, J. M., Eikmann, W., et al. 2015, *A&A*, 576, A108, doi: [10.1051/0004-6361/201425004](https://doi.org/10.1051/0004-6361/201425004)
- González-Galán, A., Negueruela, I., Castro, N., et al. 2014, *A&A*, 566, A131, doi: [10.1051/0004-6361/201423554](https://doi.org/10.1051/0004-6361/201423554)
- Grebenev, S. A., & Sunyaev, R. A. 2007, *Astronomy Letters*, 33, 149, doi: [10.1134/S1063773707030024](https://doi.org/10.1134/S1063773707030024)
- Hainich, R., Oskina, L. M., Torrejón, J. M., et al. 2020, *A&A*, 634, A49, doi: [10.1051/0004-6361/201935498](https://doi.org/10.1051/0004-6361/201935498)
- Harrison, F. A., Craig, W. W., Christensen, F. E., et al. 2013, *ApJ*, 770, 103, doi: [10.1088/0004-637X/770/2/103](https://doi.org/10.1088/0004-637X/770/2/103)
- HI4PI Collaboration, Ben Bekhti, N., Flöer, L., et al. 2016, *A&A*, 594, A116, doi: [10.1051/0004-6361/201629178](https://doi.org/10.1051/0004-6361/201629178)
- Houk, N., & Smith-Moore, M. 1988, *Michigan Catalogue of Two-dimensional Spectral Types for the HD Stars*. Volume 4, Declinations  $-26^{\circ}.0$  to  $-12^{\circ}.0$ , Vol. 4
- Hunter, J. D. 2007, *Computing in Science & Engineering*, 9, 90, doi: [10.1109/MCSE.2007.55](https://doi.org/10.1109/MCSE.2007.55)
- Huppenkothen, D., Bachetti, M., Stevens, A. L., et al. 2019a, *ApJ*, 881, 39, doi: [10.3847/1538-4357/ab258d](https://doi.org/10.3847/1538-4357/ab258d)
- . 2019b, *Journal of Open Source Software*, 4, 1393, doi: [10.21105/joss.01393](https://doi.org/10.21105/joss.01393)
- Inoue, H. 1985, *SSRv*, 40, 317, doi: [10.1007/BF00212905](https://doi.org/10.1007/BF00212905)

- Iwakiri, W., Gendreau, K., Arzoumanian, Z., et al. 2022, The Astronomer’s Telegram, 15181, 1
- James, M., Paul, B., Devasia, J., & Indulekha, K. 2010, MNRAS, 407, 285, doi: [10.1111/j.1365-2966.2010.16880.x](https://doi.org/10.1111/j.1365-2966.2010.16880.x)
- Kaur, R., Paul, B., Raichur, H., & Sagar, R. 2007, ApJ, 660, 1409, doi: [10.1086/513418](https://doi.org/10.1086/513418)
- Kobayashi, K., Negoro, H., Sugita, S., et al. 2022, The Astronomer’s Telegram, 15188, 1
- Kretschmar, P., Fürst, F., Sidoli, L., et al. 2019, NewAR, 86, 101546, doi: [10.1016/j.newar.2020.101546](https://doi.org/10.1016/j.newar.2020.101546)
- Kreykenbohm, I., Wilms, J., Kretschmar, P., et al. 2008, A&A, 492, 511, doi: [10.1051/0004-6361:200809956](https://doi.org/10.1051/0004-6361:200809956)
- Krtićka, J., & Kubát, J. 2011, A&A, 534, A97, doi: [10.1051/0004-6361/201116679](https://doi.org/10.1051/0004-6361/201116679)
- Leahy, D. A., Darbro, W., Elsner, R. F., et al. 1983, ApJ, 266, 160, doi: [10.1086/160766](https://doi.org/10.1086/160766)
- Liu, Q., Wang, W., Chen, X., et al. 2022, MNRAS, 516, 5579, doi: [10.1093/mnras/stac2646](https://doi.org/10.1093/mnras/stac2646)
- Makishima, K., Mihara, T., Nagase, F., & Tanaka, Y. 1999, ApJ, 525, 978, doi: [10.1086/307912](https://doi.org/10.1086/307912)
- Martínez-Núñez, S., Kretschmar, P., Bozzo, E., et al. 2017, SSRv, 212, 59, doi: [10.1007/s11214-017-0340-1](https://doi.org/10.1007/s11214-017-0340-1)
- Matsuoka, M., Kawasaki, K., Ueno, S., et al. 2009, PASJ, 61, 999, doi: [10.1093/pasj/61.5.999](https://doi.org/10.1093/pasj/61.5.999)
- Mihara, T., Nakajima, M., Sugizaki, M., et al. 2011, PASJ, 63, S623, doi: [10.1093/pasj/63.sp3.S623](https://doi.org/10.1093/pasj/63.sp3.S623)
- NASA High Energy Astrophysics Science Archive Research Center (HEASARC). 2014, HEASoft: Unified Release of FTOOLS and XANADU, Astrophysics Source Code Library, record ascl:1408.004. <http://ascl.net/1408.004>
- Negoro, H., Mihara, T., Pike, S., et al. 2022, The Astronomer’s Telegram, 15193, 1
- Nesci, R. 2022, The Astronomer’s Telegram, 15194, 1
- Pike, S. N., Sugizaki, M., Eijnden, J. v. d., et al. 2023, ApJ, 954, 48, doi: [10.3847/1538-4357/ace696](https://doi.org/10.3847/1538-4357/ace696)
- Pradhan, P., Bozzo, E., & Paul, B. 2018, A&A, 610, A50, doi: [10.1051/0004-6361/201731487](https://doi.org/10.1051/0004-6361/201731487)
- Prinja, R. K. 1989, MNRAS, 241, 721, doi: [10.1093/mnras/241.4.721](https://doi.org/10.1093/mnras/241.4.721)
- Rahoui, F., & Chaty, S. 2008, A&A, 492, 163, doi: [10.1051/0004-6361:200810695](https://doi.org/10.1051/0004-6361:200810695)
- Reig, P. 2011, Ap&SS, 332, 1, doi: [10.1007/s10509-010-0575-8](https://doi.org/10.1007/s10509-010-0575-8)
- Rikame, K., Paul, B., Pradhan, P., & Paul, K. T. 2022, MNRAS, 512, 4792, doi: [10.1093/mnras/stac729](https://doi.org/10.1093/mnras/stac729)
- Romano, P., Mangano, V., Ducci, L., et al. 2013, Advances in Space Research, 52, 1593, doi: [10.1016/j.asr.2013.07.034](https://doi.org/10.1016/j.asr.2013.07.034)
- Romano, P., Bozzo, E., Mangano, V., et al. 2015, A&A, 576, L4, doi: [10.1051/0004-6361/201525749](https://doi.org/10.1051/0004-6361/201525749)
- Roy, J., Agrawal, P. C., Iyer, N. K., et al. 2019, ApJ, 872, 33, doi: [10.3847/1538-4357/aafaf1](https://doi.org/10.3847/1538-4357/aafaf1)
- Serino, M., Negoro, H., Nakajima, M., et al. 2022, The Astronomer’s Telegram, 15178, 1
- Sguera, V., Bazzano, A., Bird, A. J., et al. 2006, ApJ, 646, 452, doi: [10.1086/504827](https://doi.org/10.1086/504827)
- Shakura, N., Postnov, K., & Hjalmarsdotter, L. 2013, MNRAS, 428, 670, doi: [10.1093/mnras/sts062](https://doi.org/10.1093/mnras/sts062)
- Shakura, N., Postnov, K., Sidoli, L., & Paizis, A. 2014, MNRAS, 442, 2325, doi: [10.1093/mnras/stu1027](https://doi.org/10.1093/mnras/stu1027)
- Shidatsu, M., Kawai, N., Maehara, H., et al. 2025, arXiv e-prints, arXiv:2503.21118, doi: [10.48550/arXiv.2503.21118](https://doi.org/10.48550/arXiv.2503.21118)
- Sidoli, L., Esposito, P., Motta, S. E., Israel, G. L., & Rodríguez Castillo, G. A. 2016, MNRAS, 460, 3637, doi: [10.1093/mnras/stw1246](https://doi.org/10.1093/mnras/stw1246)
- Sidoli, L., & Paizis, A. 2018, MNRAS, 481, 2779, doi: [10.1093/mnras/sty2428](https://doi.org/10.1093/mnras/sty2428)
- Sugizaki, M., Mihara, T., Serino, M., et al. 2011, PASJ, 63, S635, doi: [10.1093/pasj/63.sp3.S635](https://doi.org/10.1093/pasj/63.sp3.S635)
- Sugizaki, M., Mihara, T., Kobayashi, K., et al. 2022, PASJ, doi: [10.1093/pasj/psac059](https://doi.org/10.1093/pasj/psac059)
- Taam, R. E., Fryxell, B. A., & Brown, D. A. 1988, ApJL, 331, L117, doi: [10.1086/185248](https://doi.org/10.1086/185248)
- Takeshima, T., Dotani, T., Mitsuda, K., & Nagase, F. 1994, ApJ, 436, 871, doi: [10.1086/174964](https://doi.org/10.1086/174964)
- Torrejón, J. M., Schulz, N. S., Nowak, M. A., & Kallman, T. R. 2010, ApJ, 715, 947, doi: [10.1088/0004-637X/715/2/947](https://doi.org/10.1088/0004-637X/715/2/947)
- van der Klis, M., Stella, L., White, N., Jansen, F., & Parmar, A. N. 1987, ApJ, 316, 411, doi: [10.1086/165210](https://doi.org/10.1086/165210)
- Wang, Y. M. 1981, A&A, 102, 36
- Wilms, J., Allen, A., & McCray, R. 2000, ApJ, 542, 914, doi: [10.1086/317016](https://doi.org/10.1086/317016)
- Yuan, W., Zhang, C., Chen, Y., & Ling, Z. 2022, in Handbook of X-ray and Gamma-ray Astrophysics, 86, doi: [10.1007/978-981-16-4544-0\\_151-1](https://doi.org/10.1007/978-981-16-4544-0_151-1)